

Broadband Sensitized Near-Infrared Quantum Cutting Materials for Silicon Solar Cells: Progress, Challenges, and Perspectives

Guoxiang Song, Chaogang Lou,* Han Diao, and Ruiqi Zhu

Silicon solar cells are currently the most widely used type, accounting for more than 90% of the commercial market. However, the spectral mismatch between the solar spectrum and the absorption spectra of the cells is the main cause restricting their conversion efficiency, which cannot exceed the Shockley–Queisser limit. Quantum cutting can convert one high-energy photon into two or more low-energy photons and reduce the energy loss of the high-energy photons, providing a way to improve the photoelectric conversion efficiency (PCE) of silicon solar cells. The unique electronic configuration of rare-earth elements gives them excellent optical properties and makes them good candidates for the luminescent centers of quantum cutting materials. This article reviews their luminescence mechanism, energy transfer (ET) mechanism, and application in silicon solar cells and outlines the potential problems of broadband-sensitized near-infrared (NIR) quantum cutting materials. Some key issues and future directions are also discussed.

1. Introduction

In light of the global energy crisis and the increasing issue of environmental pollution, renewable and clean energy are essential for sustainable development.^[1–5] The ability of solar cells to convert sunlight directly into electricity makes them one of the most popular renewable energy technologies today.^[6–10] Among many solar cells, silicon solar cells occupy the primary photovoltaic market due to their mature technology, non-toxicity, long life, low cost, etc.^[11–16]

Despite the advantages of silicon solar cells, their photovoltaic conversion efficiency (PCE) is still lower than the expectation. According to the Shockley–Queisser theory,^[17] the PCE of crystalline silicon solar cells can reach up to 29.4% under ideal conditions. After the PCE of the crystalline silicon solar cells has been recorded at 26.81%,^[18] approaching the Shockley–Queisser limit, it becomes difficult to improve further the

efficiency only by the traditional methods of optimizing materials or changing the device structure.

For the silicon solar cells, since the bandgap is 1.12 eV ($\lambda = 1100$ nm), their spectral response range is 300–1100 nm.^[19–21] After the short-wave photons with the energy higher than 1.12 eV in sunlight are absorbed by the cells, the excessive energy is transformed into heat losses in the form of lattice thermalization, while the long-wave photons with lower energy transmit through the cells because they cannot excite photogenerated carriers.^[22,23] The inconsistency between the absorption spectra of the solar cells and the solar spectrum is usually called spectral mismatch, which is the main factor limiting the PCE of the silicon solar cells.^[24,25] Figure 1 shows the energy

loss processes in a single-junction solar cell. Among them, the lattice thermalization loss caused by high-energy photons and the transparency loss caused by low-energy photons are the main reasons for the energy loss of solar cells.^[26]

Quantum cutting is the process by which the materials absorb a high-energy photon and emit two or more low-energy photons.^[27–29] Quantum cutting materials can convert high-energy photons with poor photovoltaic response into more desirable low-energy photons, thus bringing a chance to break the Shockley–Queisser limit of silicon solar cells.^[30,31] In 2002, Trupe et al.^[32] theoretically predicted that, for a solar cell with an energy band of 1.1 eV, the PCE can reach 38.6% with the application of quantum cutting materials. Since then, a large number of experimental explorations have been carried out.^[33–35]

Rare-earth element ions are promising contenders for quantum cutting materials because of their abundant energy levels.^[36–38] This review will focus on their luminescence mechanism, the energy transfer (ET) mechanism, and their application in silicon solar cells. Also, some key issues and possible directions are discussed.

2. Quantum Cutting Theory

2.1. Rare-Earth Ion Luminescence

Rare-earth elements include those in the periodic table from No. 57 (lanthanum, La) to No. 71 (lutetium, Lu) and two elements,

G. Song, C. Lou, H. Diao, R. Zhu
School of Electronic Science and Engineering
Joint International Research Laboratory of Information Display and Visualization
Southeast University
Nanjing 210096, China
E-mail: lcg@seu.edu.cn

 The ORCID identification number(s) for the author(s) of this article can be found under <https://doi.org/10.1002/solr.202400026>.

DOI: 10.1002/solr.202400026

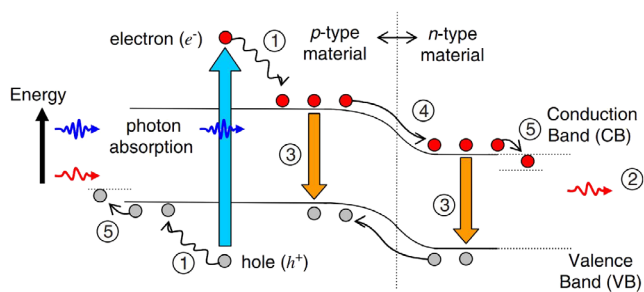


Figure 1. Energy loss processes in a single-junction solar cell: ① lattice thermalization loss; ② transparency loss; ③ recombination loss; ④ junction loss; and ⑤ contact voltage loss. Reproduced with permission.^[26] Copyright 2006, Elsevier.

scandium (Sc) and yttrium (Y), in group IIIB, a total of 17 elements. Their 4f electronic orbitals are not filled fully, and the electrons in the ground states can be excited to these orbitals by absorbing energy. These excited electrons then return to the ground state through radiative transitions by emitting photons or through nonradiative transitions. According to the rare-earth ion spectroscopy theory,^[39] the luminescence of rare-earth ions can be classified into three categories. The first is the linear spectra due to *ff* transition, which cover a wide range of spectral lines, including ultraviolet (Gd^{3+}), visible (Eu^{3+} , Dy^{3+} , Tm^{3+} , Tb^{3+} , Pr^{3+} , Sm^{3+}), and infrared (Yb^{3+} , Ho^{3+} , Nd^{3+} , Er^{3+} , Pr^{3+}). The second category is the band spectra resulting from *f-d* transition, such as the trivalent ions Pr^{3+} , Ce^{3+} , Tb^{3+} and the divalent ions Eu^{2+} , Sm^{2+} , Yb^{2+} , Tm^{2+} , Dy^{2+} , Nd^{2+} . They have large absorption cross-sections, and the emissions are also broadband but are strongly influenced by the host materials and temperature. The third category is charge transfer luminescence. When the electrons migrate from the molecular orbital of the ligand ion (oxygen or halogen) to the unfilled 4f orbitals of the rare-earth ions, the charge transfer luminescence will occur. The spectral positions of this type of ions are greatly affected by the environment, and their spectral bands are relatively broad. The trivalent ions such as Eu^{3+} , Sm^{3+} , Tm^{3+} , Yb^{3+} , and the tetravalent ions such as Ce^{4+} , Pr^{4+} , Tb^{4+} , Nd^{4+} , and Dy^{4+} undergo the charge transfer luminescence.

2.2. ET between Rare-Earth Ions

The ET between the rare-earth ions is the most critical process in which the luminescence efficiency of the quantum cutting materials depends. The sensitizer absorbs the energy and then transfers it to the activators, which are the luminescent centers. **Figure 2** lists the currently popular ways of ET between rare-earth ions.^[40] The ET occurs mainly through resonant transfer and non-resonant transfer. Resonance ET can occur when the emission spectra of the sensitizer overlap with the absorption spectra of the activator. Otherwise, only non-resonant transfer happens: a) Resonant radiative ET. If there is an overlap between the emission spectra of the sensitizer and the absorption spectra of the activator when the sensitizer and activator are far away and have no direct interaction, the photons emitted by the sensitizer may be reabsorbed by the activator; b) Resonant nonradiative ET. This transfer also requires an overlap between the emission spectra of the sensitizer and the absorption spectra of the activator. When the sensitizer and activator are close and may interact, the sensitizer may transfer the energy to the activator in a resonant nonradiative manner. The ET in this manner is relatively efficient and is the main mode of the ET; c) Phonon-assisted nonradiative ET. If there is no overlap between the emission spectra of the sensitizer and the absorption spectra of the activator, that is, the resonance condition is not met, when the energy level difference from the ground state to the excited state of the sensitizer is closer to that of activator, with the assistance of phonon energy in the matrix, the energy level matching is achieved by absorbing or emitting phonons. In this case, the phonon-assisted nonradiative ET occurs; d) Cross-relaxation. If there is an intermediate energy level of the sensitizer, the energy level difference between the excited state and the intermediate energy level is consistent with that between the ground state of the activator and its excited state, and a cross-relaxation nonradiative ET may occur between the two ions; and e) Cooperative energy transfer (CET). If the energy level difference of the sensitizer is the sum of the energy level differences of two or more activators, CET may occur; that is, one sensitizer transfers energy to two or more activators at the same time.

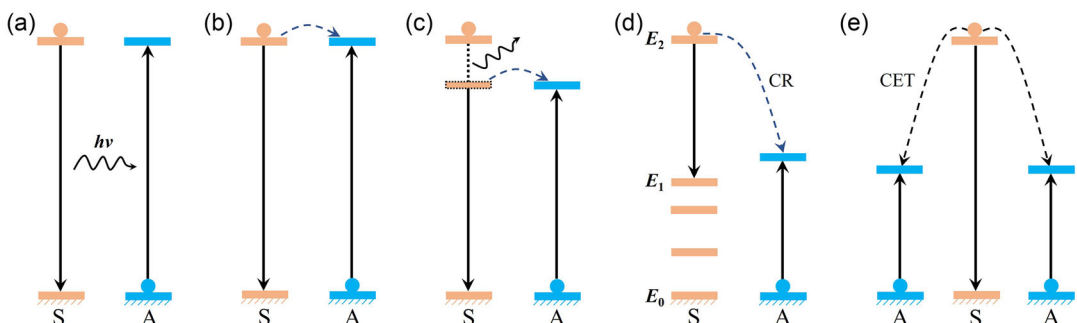


Figure 2. Mechanism of ET between the sensitizer (S) ions and the activator (A) ions. a) resonant radiative transfer, b) resonant nonradiative transfer, c) phonon-assisted nonradiative transfer, d) cross-relaxation, and e) cooperative energy transfer. Reproduced with permission.^[40] Copyright 2004, American Chemical Society.

2.3. Quantum Cutting Luminescence Mechanism

In 1957, Dexter first proposed the concept of quantum cutting and explained it theoretically,^[41] which kicked off the research. 1974, Piper et al.^[42] and Sommmerdijk et al.^[43] observed the quantum cutting luminescence in $\text{YF}_3\text{-Pr}^{3+}$ almost simultaneously, which made it officially enter the stage of spectroscopy research. In 1999, Wegh et al.^[44] reported the quantum cutting luminescence based on the two-step ET from Gd^{3+} to Eu^{3+} , which is essential work in the field.

The quantum cutting luminescence mechanism is shown in Figure 3.^[44] Figure 3a represents the cascade radiation quantum cutting of a single ion, emitting two photons. Figure 3b shows that part of the energy of the sensitizer is transferred to the ion activator by cross-relaxation, and the partial energy is transferred to another activator by energy level resonance, and finally, two activator ions each emit a photon. Figure 3c shows that the excited sensitizer transfers part of its energy to the activator through cross-relaxation and excites the activator to the excited state. Then, both ions transit to the ground states and release two photons. Figure 3d shows that the sensitizer transitions from a highly excited state to a low excited state and emits a photon, at the same time transferring the rest of the energy to the activator, which then transits back to the ground state and emits a photon. In Figure 3e, there is no intermediate energy level, and the energy is divided into two by CET, which is delivered to both activator ions at the same time, and then two photons are released. It is imperative to note here that, so far, no experiments can directly demonstrate these five quantum cutting luminescence mechanisms. This makes it challenging to apply the quantum cutting materials on the solar cells.

2.4. Rare-Earth Ions for Broadband-Sensitized NIR Quantum Cutting

Currently, the common sensitizers in quantum cutting materials are Tb^{3+} ,^[45] Pr^{3+} ,^[46] Tm^{3+} ,^[47] and Er^{3+} .^[48] However, these ions have narrow absorption bands caused by the parity forbidden

$4f-4f$ transitions. To increase the PCE of the silicon solar cells more effectively, the quantum cutting materials need to have a broad absorption band. For this purpose, Ce^{3+} and Eu^{2+} are good candidates because they have a wide $4f-5d$ absorption band, which effectively absorbs the photon energy in ultraviolet-visible regions and can be employed as sensitizers.^[49–53] Furthermore, the emission spectra of Eu^{2+} change with the different matrix materials, which is more conducive to matching the emission spectra of the sensitizer with the absorption spectra of the activator, which is very helpful in obtaining a high energy transfer efficiency (ETE).

To achieve near-infrared (NIR) emission, the most commonly used activators are Yb^{3+} and Nd^{3+} . According to the Dieke energy level,^[39] Yb^{3+} has only two energy levels ($^2\text{F}_{7/2}$ ground state and $^2\text{F}_{5/2}$ excited state) with an energy level difference of 1.27 eV (corresponding to 980 nm), which matches the bandgap of silicon, so the early quantum cutting luminescent materials applied to the silicon solar cells mainly use Yb^{3+} ions as activators.^[49,54] The energy level structure and spectra of Nd^{3+} ions are very rich and can generate NIR light at 850–1450 nm. The transitions from $^4\text{F}_{3/2}$ to $^4\text{I}_{9/2}$, $^4\text{I}_{11/2}$, and $^4\text{I}_{13/2}$ correspond to NIR emissions with peaks of about 910, 1064, and 1341 nm, respectively.^[55]

3. Broadband-Sensitized NIR Quantum Cutting Materials for Silicon Solar Cells

To be applied on the silicon solar cells, the quantum cutting materials should satisfy some requirements: 1) broad excitation spectra; 2) big absorption cross sections; 3) emission wavelength around 1000 nm; 4) high light transmittance in unabsorbed wavelength ranges; 5) high quantum efficiency (QE); 6) good stability; 7) non-toxic and non-hazardous; and 8) low fabrication costs. Due to their excellent luminescence properties, stability, and low cost, rare-earth phosphors are among the most promising quantum cutting materials.

Figure 4a shows that the quantum cutting layers are usually located above the solar cells to cut the high-energy incident

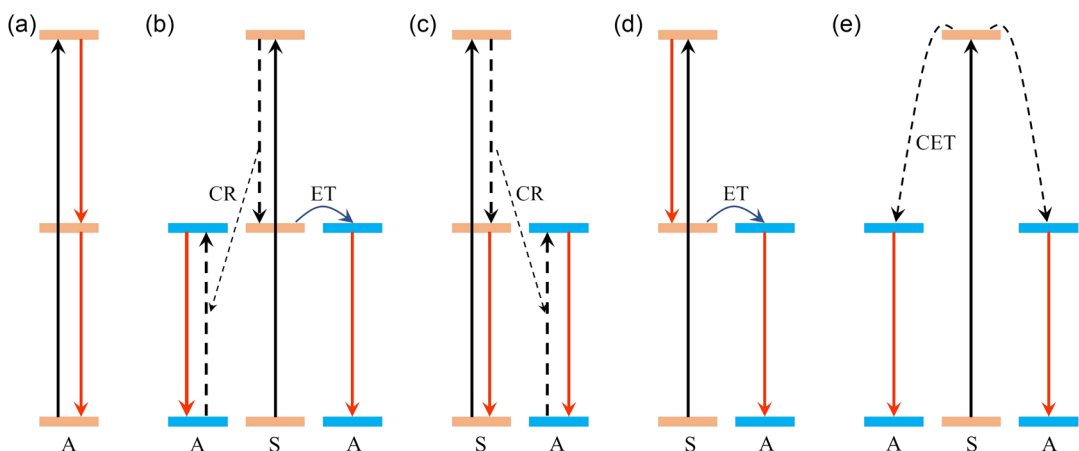


Figure 3. Schematic diagram of quantum cutting luminescence mechanism. a) Cascade emission process of a single ion, b) two-step energy transfer, c) and d) one-step energy transfer from ion S to A, and e) cooperative energy transfer. Reproduced with permission.^[44] Copyright 1999, The American Association for the Advancement of Science.

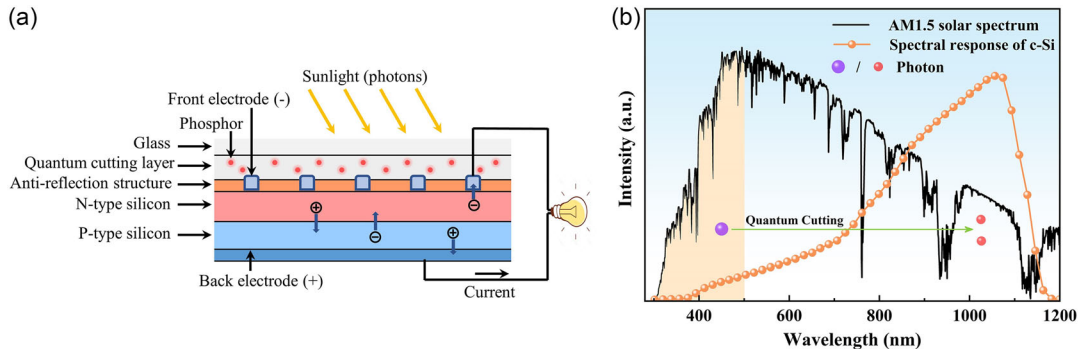


Figure 4. a) Schematic diagram of the silicon solar cell with a quantum cutting layer. b) The AM1.5 solar spectrum and spectral response of c-Si.

photons directly when applied to the solar cells. In this review, quantum cutting materials with emission wavelengths around 1000 nm are chosen to improve the efficiency of crystalline silicon solar cells for the following three main reasons: 1) We know that the spectral response of crystalline silicon solar cells in the visible range is also excellent. However, a photon in the UV-blue region can only be converted into a photon in the visible range. This phenomenon is known as down-shifting, and the QE will not exceed 100%.^[56] As shown in Figure 4b, the energy of photons around 1000 nm is lower relative to visible photons, and one photon in the UV-blue region can produce two 1000 nm near-infrared photons through quantum cutting, which can achieve a quantum efficiency of more than 100%; 2) Visible photons have higher energy than near-infrared photons, and after visible photons excite electron-hole pairs on silicon solar cells, the excess energy is lost in the form of lattice thermalization. However, photons around 1000 nm match well with the silicon bandgap and can significantly reduce this energy loss, thereby increasing the utilization of sunlight; and 3) The lattice thermalization loss caused by the action of 1000 nm photons on silicon solar cells is low, which can reduce the negative impact of high temperature on cell performance.

As shown in Figure 5, the main host matrices for quantum cutting materials are oxides,^[57] aluminates,^[58] silicates,^[59] borates,^[54] phosphates,^[60] scandates,^[61] halides,^[62] and sulfides.^[63] However, due to the complexity of the materials, the mechanism of the ET between different rare-earth ions is not easy to be clarified. Here, we review four pairs of rare-earth ion combinations, Ce³⁺-Yb³⁺, Eu²⁺-Yb³⁺, Ce³⁺-Nd³⁺, and Eu²⁺-Nd³⁺, which have broadband absorption and the NIR emission, and discuss their possible ET mechanisms, the factors affecting the QE, and the applications in the silicon solar cells.

3.1. Ce³⁺-Yb³⁺

Ce³⁺-Yb³⁺ is one of the most extensively investigated combinations for rare-earth quantum cutting materials.^[54,64] The current ET mechanism of Ce³⁺-Yb³⁺ is still controversial, and the possible ET mechanisms of Ce³⁺-Yb³⁺ are given in Figure 6. Under light excitation, $^2F_{5/2}$ ground state electrons of Ce³⁺ are excited to the higher energy level 5d, and then, through the ET process, the energy of the excited electrons is transferred to the adjacent Yb³⁺ ions, which causes Yb³⁺ ions to transition to the excited state

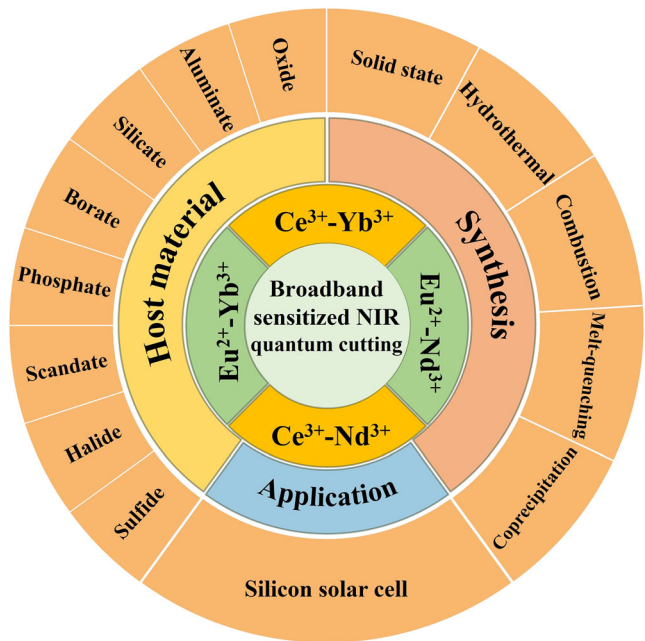


Figure 5. Summary of host materials, synthesis methods, and applications of broadband-sensitized NIR quantum cutting materials.

$^2F_{5/2}$. When Yb³⁺ ions go back to the ground state $^2F_{7/2}$, the NIR photons are emitted.

There are two possible ET mechanisms between Ce³⁺-Yb³⁺: 1) Phonon-assisted ET. During this process, Ce³⁺ loses a part of its energy and then transfers the partial energy to Yb³⁺, and Yb³⁺ releases NIR photons. It should be emphasized that this process is not quantum cutting because the number of emitted photons is not increased; and 2) CET. As shown in Figure 6, the transition energy of Ce³⁺: $5d_1 \rightarrow ^2F_{5/2}$ is twice that of Yb³⁺: $^2F_{7/2} \rightarrow ^2F_{5/2}$, so it is theoretically possible to realize the two-photon emission process of Yb³⁺ through CET. This theory has been reported in multiple literature.^[64–68] In 2012, Zhou et al.^[64] verified that when the minimum energy of the 5d excited state of the Ce³⁺ ion is close to twice the absorption energy of Yb³⁺, Ce³⁺-Yb³⁺ can realize the quantum cutting effect, and the QE is the highest. In 2019, another research group^[69] obtained similar conclusions for perovskite materials. The results reveal that the QE is the highest when the perovskite bandgap is adjusted to be close to 2 times the

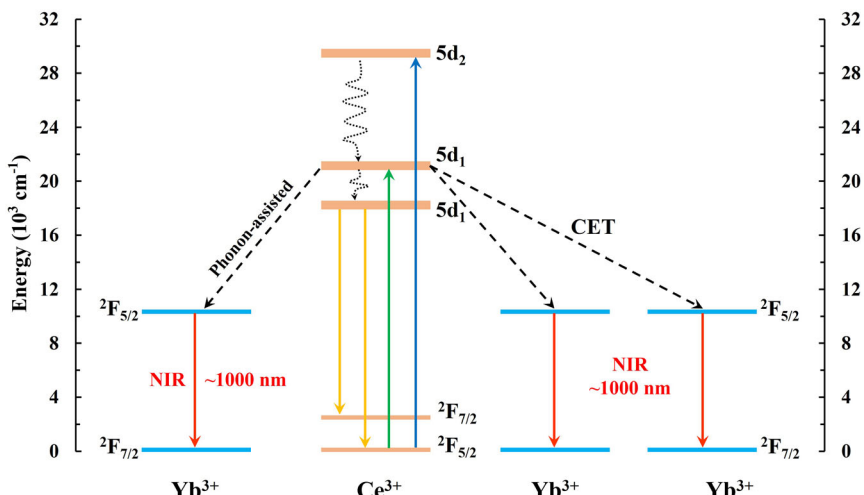


Figure 6. Schematic diagram of ET between Ce^{3+} and Yb^{3+} .

excited energy level of Yb^{3+} . In contrast, when the perovskite bandgap is below 2 times the excited energy level of Yb^{3+} , the quantum cutting process no longer occurs, and the luminescence efficiency of the Yb^{3+} ions decreases drastically. Since the energy level of the lowest 5d excited state of Ce^{3+} ions is easily affected by the crystal field of the matrix materials, it is essential to investigate the luminescence characteristics of $\text{Ce}^{3+}\text{-Yb}^{3+}$ co-doping in different matrix materials and develop the quantum cutting materials with the high QE, so that the lowest energy level of 5d excited state of Ce^{3+} ions is close to about twice the absorption energy of Yb^{3+} .

Besides the two possible ET mechanisms above, some researchers have proposed the Ce-O-Yb charge transfer state (CTS) to explain the mechanism of the ET from Ce^{3+} to Yb^{3+} (Figure 7c).^[70] Since the 5d electron of Ce^{3+} makes it easier to form a chemical bond with the adjacent O^{2-} , and the strong electronegativity of Yb makes it easier to bond Yb^{3+} and O^{2-} , it is possible to form Ce-O-Yb CTS. After a 4f electron of Ce^{3+} is excited to the 5d energy level, the electron will transit to $^2\text{F}_{5/2}$ of Yb^{3+} via CTS. Then, it relaxes to the bottom of the 5d energy level before emitting a photon. Although near-infrared photons can be emitted through the ET process of CTS,^[70,71] this process is not quantum cutting because the material absorbs one high-energy photon while only one low-energy photon can be released. Due to the down-conversion effect, this phosphor enhances the absorption of sunlight by solar cells in the short-wave range (Figure 7a,b).

Although the research on $\text{Ce}^{3+}\text{-Yb}^{3+}$ co-doped quantum cutting materials has made great progress, many problems remain to be clarified. For the quantum cutting materials co-doped with the rare-earth ions, there is no directly observable method to prove whether there is ET between the sensitizer and the activator, and all are verified by some indirect experimental phenomena. As shown in Figure 7d-f,^[72] the ET between rare-earth ions can usually be verified by the following four phenomena: 1) Yb^{3+} has only two energy levels, $^2\text{F}_{5/2}$ and $^2\text{F}_{7/2}$, and the energy level difference between them corresponds to an absorption wavelength of about 980 nm. Therefore, Yb^{3+} cannot absorb the

photons in the UV-visible region. If the co-doped materials are excited by UV or visible light, the emission of Yb^{3+} at 976 nm indicates that the ET from Ce^{3+} to Yb^{3+} occurs (Figure 7d); 2) In the excitation spectra monitored at the emission wavelength 976 nm of Yb^{3+} , there exist two absorption bands of $^2\text{F}_{5/2}\rightarrow 5d_1$ (370 nm) and $^2\text{F}_{5/2}\rightarrow 5d_2$ of Ce^{3+} (300 nm), which certify the ET from Ce^{3+} to Yb^{3+} ; 3) In Figure 7e, the emission intensity of Ce^{3+} gradually decreases with increasing Yb^{3+} concentration, which shows the ET from Ce^{3+} to Yb^{3+} ; and 4) In Figure 7f, the luminescence lifetime of Ce^{3+} decreases gradually with the increase of Yb^{3+} concentration, which also indicate the ET from Ce^{3+} to Yb^{3+} .

Notably, in Figure 7e, the emission intensity of Yb^{3+} starts to decrease when the Yb^{3+} concentration exceeds 0.02, which is attributed to the concentration quenching. When Yb^{3+} concentration in the matrix is high, the distance between adjacent Yb^{3+} ions is less than the critical distance, and the Yb^{3+} in the excited state and ground state undergoes cross-relaxation between each other. The energy is transferred from a luminescent center to another luminescent center, making the energy of the excited state continuously migrate between the central ions without radiation until it is finally transferred to the quenching center (impurities, defects, etc.), and part of the energy is lost in the form of nonradiative transitions, which greatly weakens the luminescence intensity of Yb^{3+} in the NIR region.^[68,72] How to weaken this influence is a crucial point in the area.

We can attempt to use fluorescent materials with a core-shell structure to wrap the rare-earth ions in a shell to reduce the interactions between the rare-earth ions, thereby attenuating the effect of concentration quenching. Sun et al.^[73] developed a Ce^{3+} -doped core-shell structured nanomaterial with quantum cutting effect, as shown in Figure 7g. They employed NaGdF_4 as a matrix and doped Ce^{3+} and $\text{Nd}^{3+}/\text{Yb}^{3+}$ in the core and shell layers, respectively, and successfully suppressed the fluorescence quenching induced by cross-relaxation between ions. The steady-state spectra and fluorescence lifetime studies show that the excitation energy is absorbed by Ce^{3+} in the core layer and can migrate to the shell layer through the sublattice of Gd^{3+} ,

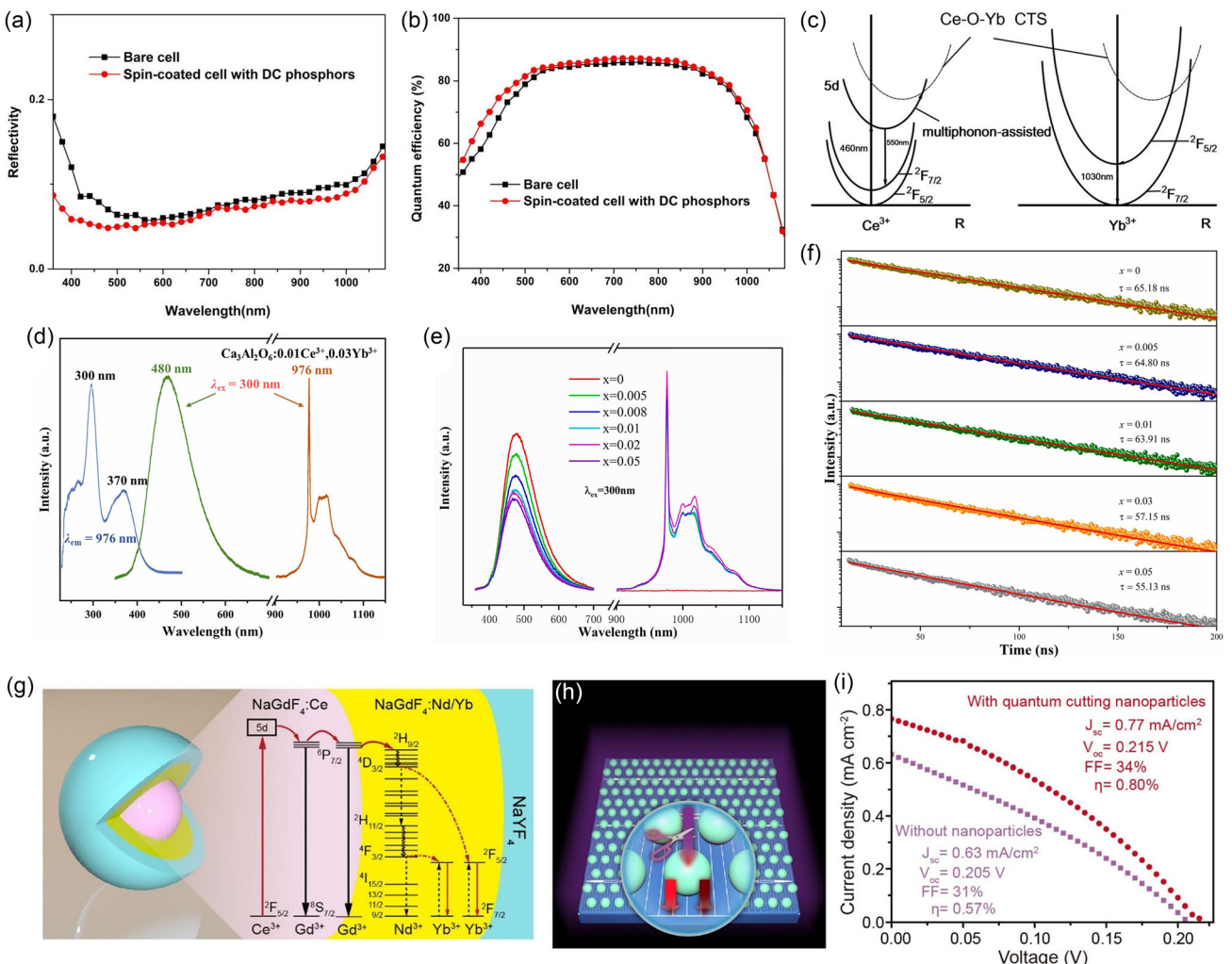


Figure 7. a) Reflectance and b) quantum efficiency of the solar cells, and c) ET process from Ce^{3+} to Yb^{3+} via Ce-O-Yb charge transfer state. Reproduced with permission.^[70] Copyright 2018, AIP Publishing. d) Excitation and emission spectra of $\text{Ca}_3\text{Al}_2\text{O}_6:\text{Ce}^{3+}$, Yb^{3+} , e) emission spectra of $\text{Ca}_3\text{Al}_2\text{O}_6:0.01\text{Ce}^{3+}$, $x\text{Yb}^{3+}$. Reproduced with permission.^[72] Copyright 2021, Elsevier. g) Schematic structure and ET process, h) schematic illustration of c-Si cells using quantum cutting nanoparticles, and i) J-V characterization of the solar cells. Reproduced with permission.^[73] Copyright 2017, American Chemical Society.

which is efficiently transferred to Nd^{3+} and Yb^{3+} . At the same time, the outermost layer can effectively inhibit the surface quenching effect by epitaxial growth of an inert layer of NaYF_4 , thereby increasing the luminescence intensity and achieving a quantum yield of up to 87%. They uniformly covered the surface of the solar cells with such nanoparticles to help the solar cells absorb ultraviolet light that would otherwise not be utilized (Figure 7h). Compared with the cells unmodified with the quantum-cutting particles, the method brought 1.2 times the short-circuit current and 1.4 times the PCE (Figure 7i). Incidentally, due to the extreme designability and scalability of this nanocore–shell structure, multiple sensitizers can be combined using the core–shell structure to further realize the quantum cutting effect of wider bandwidth sensitization.

To optimize the ET, Kumar et al.^[74] introduced Bi^{3+} ions into $\text{Y}_3\text{Al}_5\text{O}_12:\text{Ce}^{3+}\text{-Yb}^{3+}$, and successfully prepared $\text{Ce}^{3+}\text{-Bi}^{3+}\text{-Yb}^{3+}$

tri-doped phosphors. The emission spectra of $\text{Y}_3\text{Al}_5\text{O}_12:\text{Ce}^{3+}\text{-Bi}^{3+}\text{-Yb}^{3+}$ are shown in Figure 8a. The results show that the emission intensity of Yb^{3+} is intensified after doping Bi^{3+} . The ETE from Ce^{3+} to Yb^{3+} in $\text{Ce}^{3+}\text{-Bi}^{3+}\text{-Yb}^{3+}$ tri-doped phosphors was calculated to be 76.78%, higher than 63.02% of $\text{Ce}^{3+}\text{-Yb}^{3+}$ co-doped phosphors. This may be due to the fact that, in $\text{Ce}^{3+}\text{-Bi}^{3+}\text{-Yb}^{3+}$ tri-doped phosphors, the energy of Ce^{3+} can be transferred not only to Yb^{3+} but also to Bi^{3+} . Then, Bi^{3+} transfers part of the energy to Yb^{3+} . This makes Yb^{3+} gain more energy and enhances its NIR emission. To further investigate the ET between $\text{Ce}^{3+}\text{-Bi}^{3+}\text{-Yb}^{3+}$, $\text{Ce}^{3+}\text{-Bi}^{3+}$, and $\text{Bi}^{3+}\text{-Yb}^{3+}$ co-doped phosphors were prepared, and the ETE were calculated, which were 14.31% and 24.95%, respectively. The schematic diagram of ET in $\text{Y}_3\text{Al}_5\text{O}_12:\text{Ce}^{3+}\text{-Bi}^{3+}\text{-Yb}^{3+}$ is shown in Figure 8b.

Besides Bi^{3+} ions, Tb^{3+} ^[58,59,75] and Pr^{3+} ^[76] are also used as bridges for the ET between $\text{Ce}^{3+}\text{-Yb}^{3+}$ to enhance the NIR

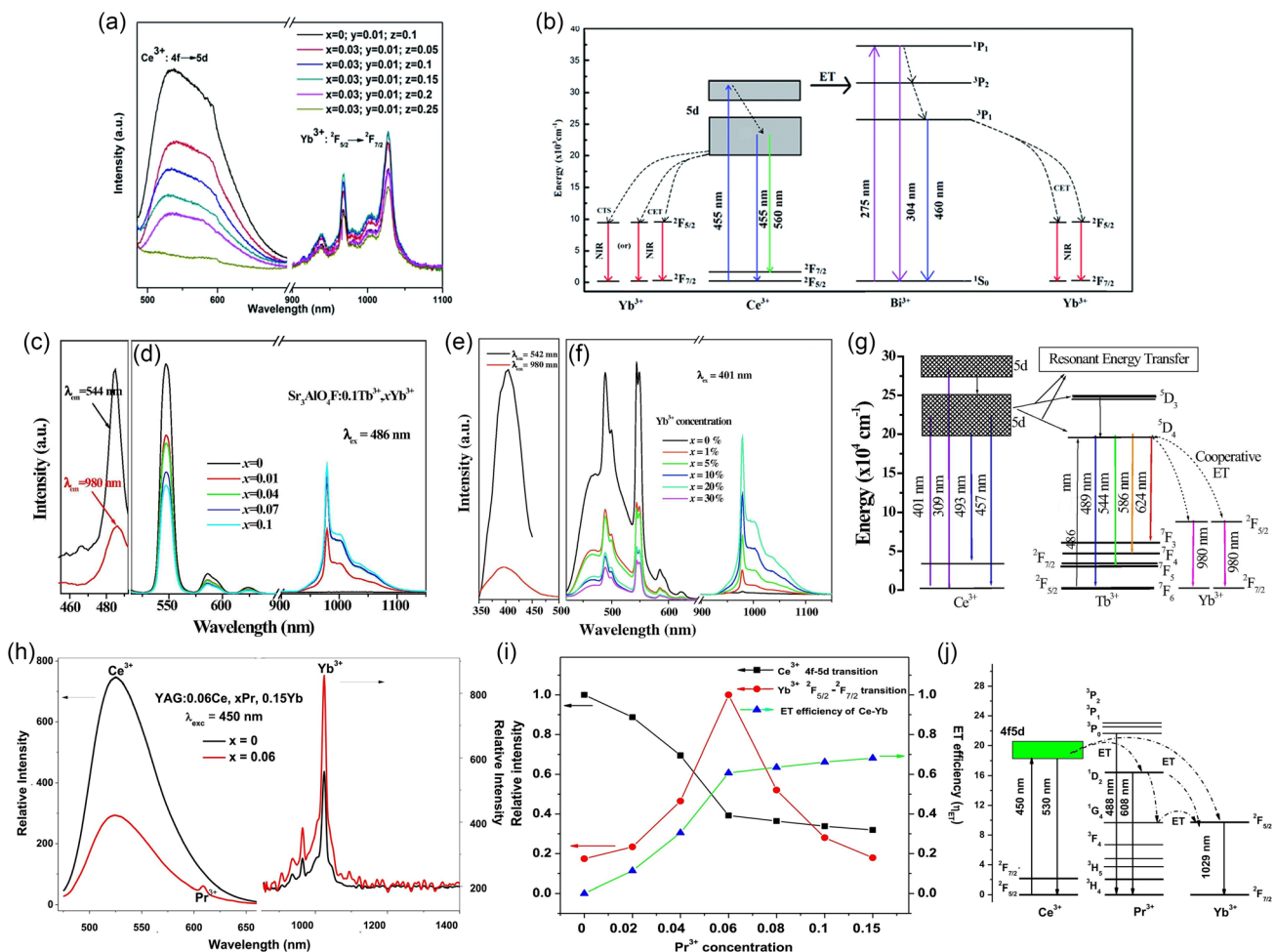


Figure 8. a) Emission spectra of $\text{Y}_3\text{Al}_5\text{O}_{12}:\text{Ce}^{3+}, \text{Bi}^{3+}, \text{Yb}^{3+}$ under the 455 nm excitation and b) schematic diagram of ET in $\text{Y}_3\text{Al}_5\text{O}_{12}:\text{Ce}^{3+}, \text{Bi}^{3+}, \text{Yb}^{3+}$. Reproduced with permission.^[74] Copyright 2017, The Royal Society of Chemistry. c) Excitation spectra of $\text{Sr}_3\text{AlO}_4\text{F}: \text{Tb}^{3+}, \text{Yb}^{3+}$, d) emission spectra of $\text{Sr}_3\text{AlO}_4\text{F}: 0.1\text{Tb}^{3+}, \text{xYb}^{3+}$, e) excitation spectra of $\text{Sr}_3\text{AlO}_4\text{F}: 0.01\text{Ce}^{3+}, 0.1\text{Tb}^{3+}, 0.01\text{Yb}^{3+}$, f) emission spectra of $\text{Sr}_3\text{AlO}_4\text{F}: 0.01\text{Ce}^{3+}, 0.1\text{Tb}^{3+}, \text{xYb}^{3+}$, and g) Schematic diagram of ET in $\text{Sr}_3\text{AlO}_4\text{F}: \text{Ce}^{3+}, \text{Tb}^{3+}, \text{Yb}^{3+}$. Reproduced with permission.^[58] Copyright 2014, Elsevier. h) Emission spectra of $\text{YAG}: 0.06\text{Ce}^{3+}, \text{xPr}^{3+}, 0.15\text{Yb}^{3+}$, i) Ce^{3+} and Yb^{3+} emission intensity and $\text{Ce}^{3+} \rightarrow \text{Yb}^{3+}$ ETE versus Pr^{3+} concentration, and j) schematic diagram of ET in $\text{YAG}: \text{Ce}^{3+}, \text{Pr}^{3+}, \text{Yb}^{3+}$. Reproduced with permission.^[76] Copyright 2017, Elsevier.

emission of Yb^{3+} . Sun et al.^[58] investigated the ET between Ce^{3+} , Tb^{3+} , and Yb^{3+} in $\text{Sr}_3\text{AlO}_4\text{F}$. In Figure 8c, the strong absorption peak at 485 nm is attributed to $\text{Tb}^{3+}: ^5F_6 \rightarrow ^5D_4$. There are three peaks in the visible region in Figure 8d, which are located at 544, 586, and 624 nm and correspond to $\text{Tb}^{3+}: ^5D_4 \rightarrow ^7F_5$, $^5D_4 \rightarrow ^7F_4$, and $^5D_4 \rightarrow ^7F_3$, respectively. The emission at 980 nm is attributed to $\text{Yb}^{3+}: ^2F_{5/2} \rightarrow ^2F_{7/2}$. It is also observed that the emission of Yb^{3+} is gradually enhanced with the increase of Yb^{3+} concentration. In the excitation spectrum of $\text{Sr}_3\text{AlO}_4\text{F}: \text{Ce}^{3+}, \text{Tb}^{3+}, \text{Yb}^{3+}$ in Figure 8e, a broad excitation peak of $\text{Ce}^{3+}: 4f \rightarrow 5d$ at 401 nm is observed monitoring at 542 nm for the Tb^{3+} transition, which provides the evidence of the ET from Ce^{3+} to Yb^{3+} through Tb^{3+} . In the emission spectra shown in Figure 8f, the emission peaks of Ce^{3+} , Tb^{3+} , and Yb^{3+} appeared simultaneously under 401 nm excitation. Taking into account that the first-order resonance ET process ($\text{Ce}^{3+} \rightarrow \text{Tb}^{3+}$) has a higher probability than the second-order process ($\text{Ce}^{3+} \rightarrow \text{Yb}^{3+}$), the process

$\text{Ce}^{3+} \rightarrow \text{Tb}^{3+} \rightarrow \text{Yb}^{3+}$ dominates in the ET process.^[58] The ET process of $\text{Ce}^{3+} \rightarrow \text{Tb}^{3+} \rightarrow \text{Yb}^{3+}$ is shown in Figure 8g, where Ce^{3+} transfers energy to Tb^{3+} through resonance ET. The energy of $\text{Tb}^{3+}: ^5D_4 \rightarrow ^7F_6$ is about twice that of $\text{Yb}^{3+}: ^2F_{7/2} \rightarrow ^2F_{5/2}$, and Tb^{3+} transfers the energy to two different Yb^{3+} via CET.

Han et al.^[76] investigated the effect of Pr^{3+} on the $\text{Ce}^{3+} \rightarrow \text{Yb}^{3+}$ ETE in a YAG matrix. In Figure 8h, the doping of Pr^{3+} enhances the emission of Yb^{3+} at 1029 nm. Figure 8i shows the emission intensity of Ce^{3+} and Yb^{3+} and the ETE of $\text{Ce}^{3+} \rightarrow \text{Yb}^{3+}$ under different Pr^{3+} doping concentrations. It can be observed that the ETE of $\text{Ce}^{3+} \rightarrow \text{Yb}^{3+}$ increases with the growth of Pr^{3+} concentration. The above results reveal that Pr^{3+} plays a bridging role in the ET process of $\text{Ce}^{3+} \rightarrow \text{Yb}^{3+}$. From the energy level diagram in Figure 8j, there are two possible pathways for the ET from Ce^{3+} to $\text{Yb}^{3+}: \text{Ce}^{3+} \rightarrow \text{Yb}^{3+}$ and $\text{Ce}^{3+} \rightarrow \text{Pr}^{3+} \rightarrow \text{Yb}^{3+}$, which significantly augment the NIR emission efficiency of Yb^{3+} .

Although the triple-doped system can enhance the NIR emission of Yb^{3+} and Nd^{3+} , there is no literature report on the calculation method of the ETE in the triple-doped system. Therefore, exploring the ETE of the triple-doped system is an urgent issue to be solved.

As for the application, the effect of the quantum cutting materials on the silicon solar cells depends to a large extent on the reflectivity of the quantum cutting layers. How to reduce the reflectivity of the quantum cutting layers is also an important research topic at present. Karunakaran et al.^[77] mixed YAG: Ce^{3+} - Yb^{3+} phosphors with ethyl vinyl acetate (EVA) and coated it on the upper surface of the monocrystalline silicon solar cells by spin coating to improve their PCE. Figure 9a presents the fluorescence spectra of single-doped Ce^{3+} and Ce^{3+} - Yb^{3+} co-doped YAG. Figure 9b shows the reflectivity and external quantum efficiency (EQE) of the bare solar cells and the cell spin-coated EVA quantum cutting layers. It can be seen that the reflectivity of the spin-coated cell decreases across the entire wavelength band, especially in the short-wave portion. Due to the absorption of short-wave photons by YAG: Ce^{3+} - Yb^{3+} phosphors, visible and NIR photons are then emitted. A significant reduction in reflectivity was also observed in the 920–1100 nm range, which was probably attributed to the absorption of NIR by Yb^{3+} . Also, the refractive index of EVA is around 1.5, which is just between the refractive index of air and silicon (1 for air and 3.4 for silicon), resulting in a gradient change of the refractive index on the surface. The gradient refractive index can reduce the reflectivity of the surface, so the spin-coated EVA quantum cutting layers result in a reduction in the reflectivity of the cells across the entire wavelength. It can be seen from the EQE that the performance of the

cells with the spin-coated EVA quantum cutting layers is better than that of the bare cells in both the short-wave region and the NIR region, which is consistent with the reflectivity curve. Besides, the J - V characteristics of bare cells and cells spin-coated with EVA quantum cutting layers were tested (Figure 9c). After spin-coating the EVA quantum cutting layers, the PCE was increased from 15.96% of the bare cell to 16.63%, a relative increase of 4.19%, which is the result of the combined effect of the decrease in the reflectivity and the increase in the quantum cutting effect.

Additionally, Liu et al.^[68] synthesized CaF_2 hollow spherical phosphors doped with Ce^{3+} and Yb^{3+} by hydrothermal method and added them to SiO_2 solution to obtain an anti-reflection coating with quantum cutting properties. In Figure 9d, the CaF_2 :0.5% Ce^{3+} - Yb^{3+} emits visible light at 300–350 nm and NIR light at 900–1100 nm under 300 nm excitation. The CaF_2 : Ce^{3+} - Yb^{3+} anti-reflection coating with the quantum cutting properties can effectively improve the PCE by 0.16%, 0.50%, and 1.20% over the CaF_2 : Ce^{3+} anti-reflection coating, SiO_2 anti-reflection coating, and pure glass (Figure 9e). The EQE was tested to further confirm the effect of the materials (Figure 9f). The test results are consistent with Figure 9e, and the EQE of the cell containing CaF_2 : Ce^{3+} - Yb^{3+} coating is obviously elevated in both visible and NIR regions, and the enhancement is evidently better than that of CaF_2 : Ce^{3+} , SiO_2 , and pure glass. The results revealed that Ce^{3+} - Yb^{3+} doping could improve the photovoltaic performance of the silicon solar cells, which was explained by the absorption of UV light by Ce^{3+} sensitizing Yb^{3+} to emit NIR light and intensified the light absorption of the silicon solar cells.

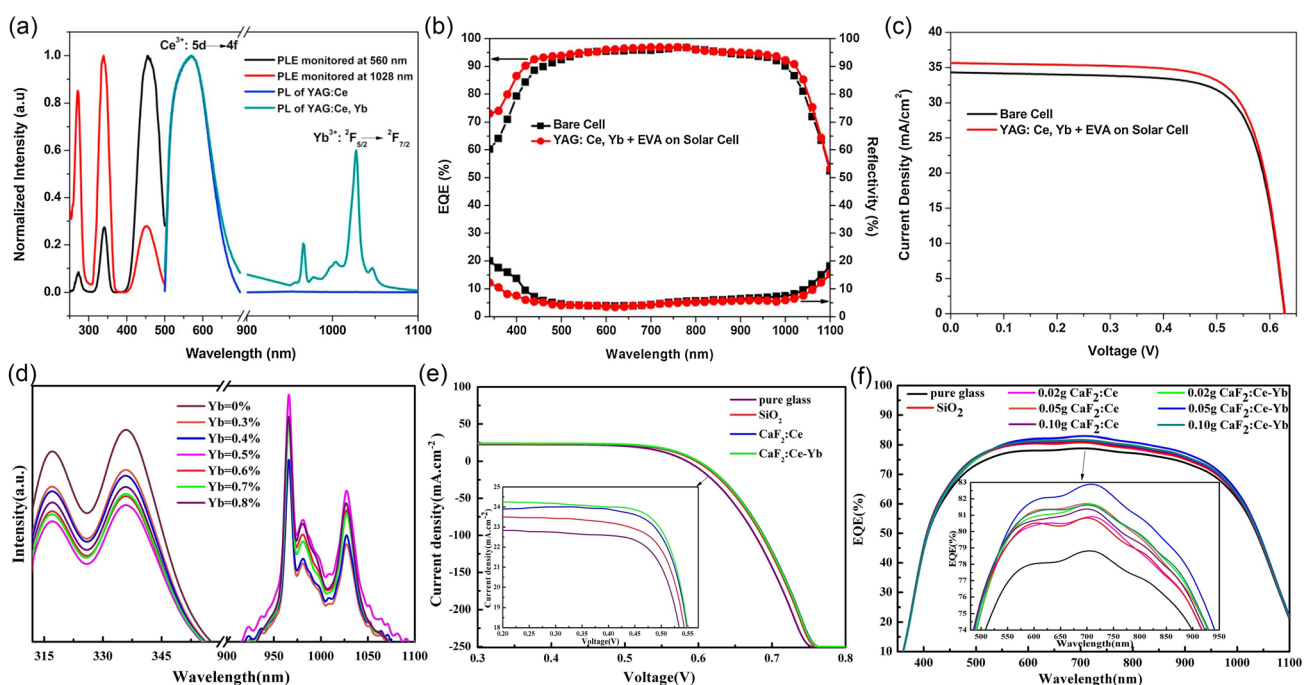


Figure 9. a) Excitation and emission spectra of single-doped Ce^{3+} and Ce^{3+} - Yb^{3+} co-doped YAG, b) reflectivity and EQE spectra, and c) J - V characteristics of the bare cell and the solar cell with YAG:Ce,Yb. Reproduced with permission.^[77] Copyright 2019, Elsevier. d) Emission spectra of CaF_2 :0.5% Ce^{3+} , Yb^{3+} , e) comparison of the J - V characteristics of different anti-reflection coatings, and f) EQE of silicon solar cells with anti-reflection layers. Reproduced with permission.^[68] Copyright 2016, Elsevier.

As can be seen from the above examples, the combination of the quantum cutting layers and the anti-reflection structure can significantly improve the PCE of the cells. The development of more efficient anti-reflection structures is essential for the development of silicon solar cells. Yet, little research has been done to combine the quantum cutting layers with the anti-reflection structures, and more effort is needed in this area.

Microcrystalline glass is also a popular matrix for quantum cutting materials. By melt quenching, Tai et al.^[65] prepared Ce³⁺-Yb³⁺ co-doped YAG nanocrystalline glass-ceramics. The bandgap of Ce³⁺:5d₁→4f transition is twice that of Yb³⁺:2F_{7/2}→2F_{5/2}, and an incident photon absorbed by Ce³⁺ can be converted into two NIR photons at around 1000 nm by Yb³⁺, and fully utilized by the silicon solar cells. Broadband-sensitized NIR quantum cutting is achieved through the cooperative ET process from Ce³⁺ to Yb³⁺, with a QE as high as 177.8%. Zhang et al.^[78] applied Ce³⁺-Yb³⁺ co-doped oxyfluoride glass ceramics to the surface of silicon solar cells to achieve an improvement in PCE. Chen et al.^[67] achieved quantum cutting in Ce³⁺-Yb³⁺ co-doped borate glass and obtained a quantum efficiency of up to 174.1%.

Table 1 summarizes the research of Ce³⁺-Yb³⁺ co-doped NIR rare-earth doped quantum cutting materials in recent years, where λ_{ex} is the excitation wavelength, λ_{em} is the NIR emission wavelength, ETE is the energy transfer efficiency, QE is the quantum efficiency, and $\Delta\text{PCE}_{\text{QC}}$ is the relatively improved PCE after using the quantum cutting materials.

3.2. Eu²⁺-Yb³⁺

Although a large number of studies have demonstrated that broadband-sensitized NIR quantum cutting luminescent materials co-doped with Ce³⁺-Yb³⁺ can effectively upgrade the PCE of the crystalline silicon solar cells, there is a problem of the

insufficient photon utilization between the two absorption peaks of ${}^2\text{F}_{5/2}\rightarrow 5d$ and ${}^2\text{F}_{7/2}\rightarrow 5d$ of Ce³⁺. Eu²⁺ has a single-peak broader excitation band and can offset the shortage. Therefore, Eu²⁺-Yb³⁺ co-doping has also become a typical combination of the rare-earth ions in broadband-sensitized NIR quantum cutting luminescent materials.^[52,53,79,80]

As shown in **Figure 10**, there is no spectral overlap between Eu²⁺ and Yb³⁺, and the transition energy of Eu²⁺:4f⁶5d¹→4f⁷ is about twice that of Yb³⁺:2F_{7/2}→2F_{5/2}, it is impossible for a Eu²⁺ to transfer all its own energy to a Yb³⁺ through the resonant radiative or resonant nonradiative ET. Furthermore, Eu²⁺ has no intermediate energy level, so the cross-relaxation cannot occur. There are two possible ways of ET between Eu²⁺ and Yb³⁺: 1) Phonon-assisted ET. In this process, Eu²⁺ loses part of its energy and then transfers the rest of the energy to Yb³⁺, which releases a single NIR photon; and 2) CET. As seen from Figure 10, the energy of Eu²⁺:4f⁶5d¹→4f⁷ transition is close to twice that of Yb³⁺:2F_{7/2}→2F_{5/2}. Therefore, Eu²⁺ may transfer energy to two nearby Yb³⁺ at the same time by the CET, and the Yb³⁺ ion emits two NIR photons at about 1000 nm (${}^2\text{F}_{5/2}\rightarrow 2\text{F}_{7/2}$), thereby achieving NIR quantum cutting.

The quantum cutting materials co-doped with Eu²⁺-Yb³⁺ have been investigated to explore the ET mechanism. Tai et al.^[81] realized NIR quantum cutting in SrAl₂O₄:Eu²⁺, Yb³⁺ under the UV excitation at 370 nm. Both visible and NIR emission peaks appear in the emission spectra (**Figure 11b**), where the broad spectral emission peak at 450–600 nm in the visible region belongs to the Eu²⁺:4f⁶5d¹→4f⁷ transition, while the emission peak located at 900–1100 nm in the NIR region is attributed to the Yb³⁺:2F_{5/2}→2F_{7/2} transition. In Figure 11a, the profiles of the excitation spectra of Eu²⁺ ($\lambda_{\text{em}} = 515$ nm) and Yb³⁺ ($\lambda_{\text{em}} = 980$ nm) are basically the same, but careful observation reveals that the excitation spectra of Yb³⁺ still has a faint excitation peak at 266 nm. A Gaussian fit of the excitation spectra of

Table 1. Current status of the research on Ce³⁺-Yb³⁺ co-doped NIR rare-earth doped quantum cutting materials.

Couple	Host	Preparation method	λ_{ex} [nm]	λ_{em} [nm]	ETE [%]	QE (%)	$\Delta\text{PCE}_{\text{QC}}$ [%]	References
Ce ³⁺ -Yb ³⁺	YAG	Solid state	460	1030	–	–	6.04	[70]
	YAG	Solid state	460	1030	–	–	–	[71]
	Ca ₃ Al ₂ O ₆	Solid state	300	976	42.19	–	–	[72]
	YAG	Solid state	455	1028	–	–	4.19	[77]
	CaF ₂	Hydrothermal	336	965	–	–	1.20	[68]
	YAG	Melt-quenching	460	980	77.8	177.8	–	[65]
	Y ₂ SiO ₅	Solid state	372	977	94	194	–	[64]
	YAG	Co-precipitation	458	1030	91.2	191.2	–	[66]
	Oxyfluoride glass-ceramics	Melt-quenching	430	1010	–	–	0.3	[78]
	Borate glasses	Melt-quenching	330	976	74.1	174.1	–	[67]
Eu ²⁺ -Yb ³⁺	Glasses	Melt-quenching	405	980	53.4	153.4	–	[103]
	LuBO ₃	Hydrothermal	369	971	–	181	–	[51]
	YBO ₃	Solid state	358	973	–	175	–	[104]
	YBO ₃	Hydrothermal	360	971	41.9	141.9	0.521	[50]
	GaBO ₃	Solid state	358	971	64	164	–	[54]
	YAG	Solid state	469	992	–	145.9	–	[49]
	NaSrBO ₃	Solid state	350	981	48.65	–	–	[105]

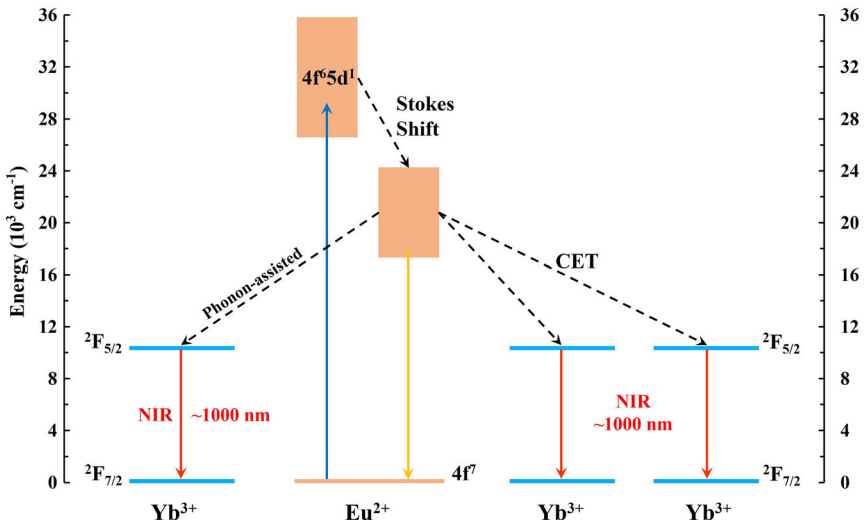


Figure 10. Schematic diagram of ET between Eu^{2+} and Yb^{3+} .

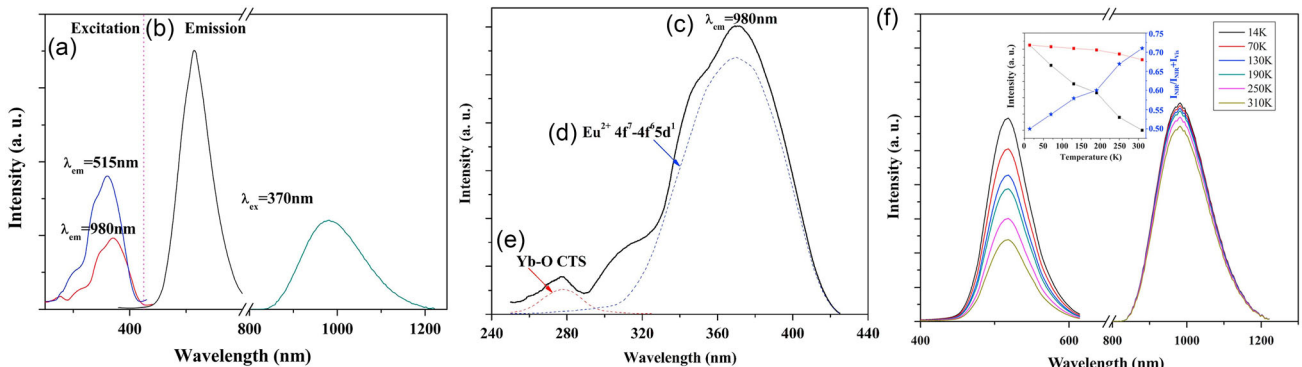


Figure 11. a) Excitation and b) emission spectra of $\text{SrAl}_2\text{O}_4:0.01\text{Eu}^{2+}, 0.01\text{Yb}^{3+}$, c) excitation spectra of $\text{SrAl}_2\text{O}_4:0.01\text{Eu}^{2+}, 0.01\text{Yb}^{3+}$ ($\lambda_{\text{em}} = 980 \text{ nm}$), d) $\text{Eu}^{2+}:4f^7 \rightarrow 4f^65d^1$ and e) Yb-O CTS by Gaussian fitting, and f) temperature-dependent emission spectra ($\lambda_{\text{ex}} = 370 \text{ nm}$) in $\text{SrAl}_2\text{O}_4:0.01\text{Eu}^{2+}, 0.20\text{Yb}^{3+}$. Reproduced with permission.^[81] Copyright 2015, Elsevier.

Yb^{3+} (Figure 11c) reveals that the excitation spectra of Yb^{3+} can be decomposed into two peaks (Figure 11d,e). The strong peak at 370 nm is attributed to the $\text{Eu}^{2+}:4f^7 \rightarrow 4f^65d^1$ transition, while the weak peak at 266 nm is attributed to the charge transfer luminescence between $\text{O}^{2-}-\text{Yb}^{3+}$, which is consistent with the existing reports.^[82] To further investigate the ET mechanism between $\text{Eu}^{2+}-\text{Yb}^{3+}$, the emission spectra of different Yb^{3+} doping concentrations were tested. Similar to the $\text{Ce}^{2+}-\text{Yb}^{3+}$ co-doping, the concentration quenching of Yb^{3+} also occurred in $\text{SrAl}_2\text{O}_4:\text{Eu}^{2+}, \text{Yb}^{3+}$ phosphors, which confirmed the ET process between $\text{Eu}^{2+}-\text{Yb}^{3+}$.

Tai et al.^[81] experimentally verified the phonon-assisted ET between $\text{Eu}^{2+}-\text{Yb}^{3+}$ in $\text{SrAl}_2\text{O}_4:\text{Eu}^{2+}, \text{Yb}^{3+}$. As shown in Figure 11f, a variable temperature fluorescence test was performed to verify whether the phonon-assisted nonradiative transitions are involved in the ET process. It can be seen that the luminescence intensity of Eu^{2+} in the visible region and that of Yb^{3+} in the NIR region gradually increases as the temperature decreases, which indicates that the phonon-assisted nonradiative

transitions are involved in the quantum cutting between $\text{Eu}^{2+}-\text{Yb}^{3+}$. Because the vibration amplitude of the lattice decreases as the temperature decreases, when the temperature is close to absolute zero, the amplitude of the lattice near the equilibrium position is almost zero, which does not lead to the nonradiative transitions, and the energy loss decreases to make the luminescence intensity of Eu^{2+} and Yb^{3+} increase. It was also noticed that although the luminescence intensity of both Eu^{2+} and Yb^{3+} decreased with increasing temperature, the decrease of Eu^{2+} was much higher than that of Yb^{3+} . This is due to the fact that Yb^{3+} has only two energy levels, $2F_{5/2}$ and $2F_{7/2}$, and the energy level difference is as high as $10\,000 \text{ cm}^{-1}$, which leads to a lower probability of the phonon-assisted nonradiative transitions, so brings a relatively small impact on the luminescence intensity of Yb^{3+} . In contrast, Eu^{2+} itself has a broad spectral luminescence of $4f \rightarrow 5d$, and the energy level splitting occurs in the SrAl_2O_4 crystal field, so the probability of nonradiative transitions is relatively high, and the luminescence intensity is significantly impacted by temperature. Therefore, it can be

speculated that the CET may dominate the ET between Eu^{2+} and Yb^{3+} . The phonon-assisted nonradiative transitions may also be involved in the process, resulting in energy loss and weakening the luminescence intensity of Eu^{2+} and Yb^{3+} .

Temperature quenching greatly influences the luminescence intensity of rare-earth ions, but there is no better way to solve the temperature quenching problem, which is a difficulty in the research. However, we can use the quantum cutting effect to minimize the temperature quenching caused by the thermal effect of sunlight on the solar cells.

Yan et al.^[80] analyzed the ET process between the rare-earth ions in more detail from the perspective of molecular polarity. Unlike most of the reports that use the phosphors as the luminescent materials, they used $\text{Eu}^{2+}\text{-Yb}^{3+}$ co-doped sulfur halide glasses. In Figure 12a, compared with the single-doped Yb^{3+} (G0) and single-doped Eu^{2+} (G1) samples, the $\text{Eu}^{2+}\text{-Yb}^{3+}$ co-doped sample (G2) shows enhanced NIR emission and reduced emission in the blue region, which means that there is likely to be an ET from Eu^{2+} to Yb^{3+} . Figure 12b shows the luminescence decay curves of the samples with different Yb^{3+} concentrations, and the ETE reaches a maximum of 85% when the Yb^{3+} concentration is 0.5 mol%. However, this value was obtained only by considering ion-ion interactions and should be considered as an upper limit for the ETE. To further explore the process of ET, Yan et al.^[80] analyzed the ETE from the perspective of molecular polarity. As we know, the ET process can be divided into two types: exchange interaction and multipole interaction. For the exchange interaction model, the standard distance between the activator and sensitizer should

be less than 0.3–0.4 nm. Due to the low doping concentration, the distance R_0 between Eu^{2+} and Yb^{3+} in this sample may be larger than the critical distance. Therefore, the ET mechanism involved most likely belongs to the multipolar interaction between the two ions.^[83] According to the ET equation of Dexter's multipolar interaction and the Reisfeld approximate theory, the following relationship can be obtained^[63,83,84]

$$\frac{\tau_0}{\tau} \propto C^{\frac{n}{2}} \quad (1)$$

where τ_0 and τ are the luminescence quantum efficiency of Eu^{2+} in the cases of undoped and doped Yb^{3+} , respectively (here, the luminescence quantum efficiency is replaced by the luminescence intensity at 433 nm); C is the concentration of Yb^{3+} ; the value of n is 6, 8, and 10 corresponding to the dipole-dipole, dipole-quadrupole, and quadrupole-quadrupole interactions, respectively. Figure 12c shows the linear fit of τ_0/τ to the square of the Yb^{3+} concentration. The good fit ($R^2 = 99.10\%$) indicates that the ET from Eu^{2+} to Yb^{3+} in the $\text{Eu}^{2+}\text{-Yb}^{3+}$ co-doped glass is the dipole-dipole interaction. In general, the dipole-dipole interaction is the most efficient among various multipole interactions, which also explains the higher ETE from Eu^{2+} to Yb^{3+} .

As we know, QE is a key indicator for evaluating quantum cutting materials. It is crucial to pick out the materials with a high QE among the many quantum cutting materials. For the calculation of QE, nonradiative energy losses caused by defects and impurities are usually neglected, and the fluorescence quantum efficiency of the sensitizer at room temperature is approximated

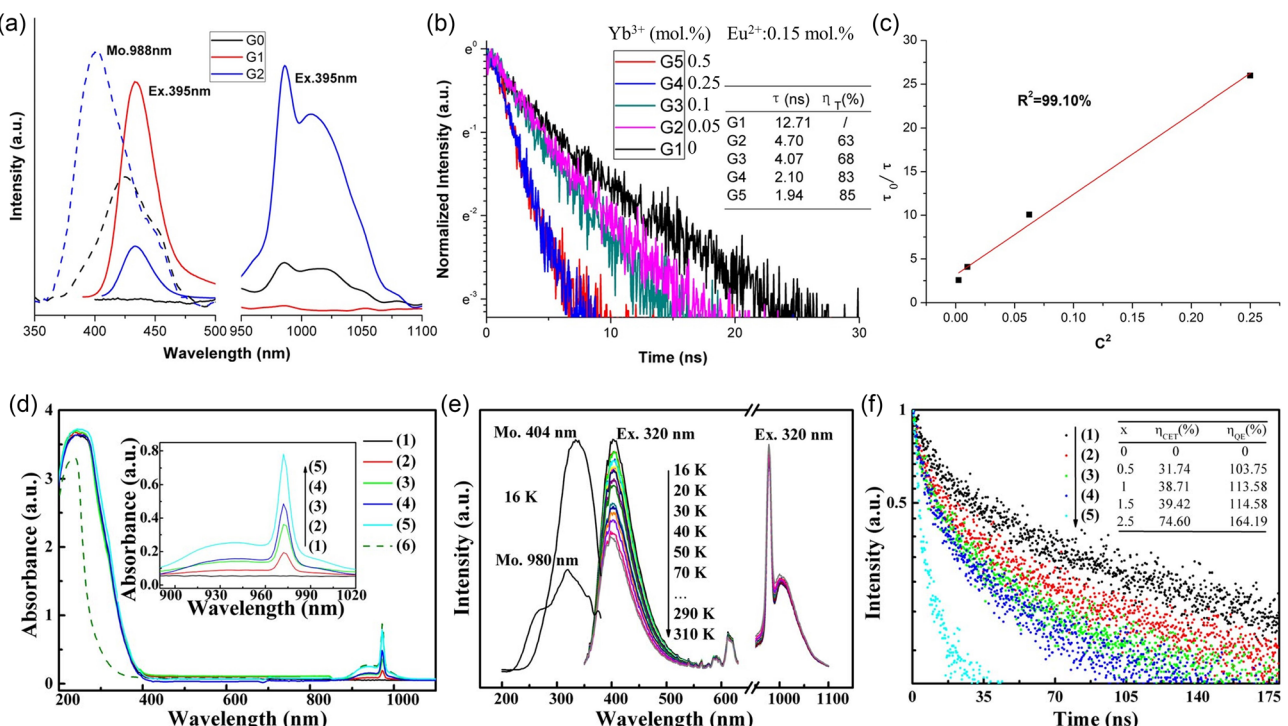


Figure 12. a) Excitation (dashed line) and emission spectra (solid line), b) luminescence decay curves of samples with different Yb^{3+} concentrations, and c) linear fit of (τ_0/τ) to the squared Yb^{3+} concentration. Reproduced with permission.^[80] Copyright 2013, The American Ceramic Society. d) Absorption spectra of the samples, e) excitation and emission spectra for various temperatures, and f) luminescence decay curves of Eu^{2+} at 404 nm emission. Reproduced with permission.^[86] Copyright 2009, AIP Publishing.

to be 100%.^[79,82,85] However, it can be seen from the previous analysis that the temperature quenching has an enormous influence on the luminescence intensity, especially for the rare-earth ions with *f-d* transition, which seriously affects the accuracy of the QE calculation. Zhou et al.^[86] performed temperature-dependent fluorescence spectroscopy analysis on Eu²⁺-Yb³⁺ co-doped borate glass samples to calculate the QE more accurately at room temperature. Figure 12d shows the absorption spectra of the samples. In Figure 12e, the luminescence intensity of Eu²⁺ gradually decreases with increasing temperature, which is attributed to the temperature quenching effect. Assuming that the fluorescence quantum efficiency of Eu²⁺ at 16 K is 1, the fluorescence quantum efficiency of Eu²⁺ (η_{Eu}) at room temperature is calculated from the proportional relationship of fluorescence intensity as 0.59. For Yb³⁺, its NIR luminescence intensity hardly changes with temperature, and thus, the fluorescence quantum efficiency of Yb³⁺ (η_{Yb}) at room temperature is considered as 1. Figure 12f shows the luminescence decay curve of Eu²⁺ at 404 nm under 320 nm excitation. With the increase of Yb³⁺ concentration, the monoexponential nature of the fluorescence decay curve of Eu²⁺ at 404 nm becomes worse due to the existence of the ET from Eu²⁺ to Yb³⁺, which introduces a Yb³⁺-related fluorescence decay pathway. The following equation can calculate the average lifetime of Eu²⁺ luminescence^[60]

$$\tau = \frac{1}{I_0} \int_0^\infty I(t) dt \quad (2)$$

where I_0 represents the luminescence intensity at the time $t = 0$. τ is the average lifetime, which is equal to the integrated area under the decay curve normalized by the intensity at $t = 0$.

The ETE between Eu²⁺→Yb³⁺ can be calculated according to the following formula^[60,86,87]

$$\eta_{\text{ETE}} = 1 - \frac{\tau_x}{\tau_0} \quad (3)$$

where τ_x and τ_0 are the average lifetime of Eu²⁺ luminescence when Yb³⁺ doping concentration is x and 0, respectively.

The theoretical QE can be calculated according to the following equation^[86,87]

$$\eta_{\text{QE}} = \eta_{\text{Eu}}(1 - \eta_{\text{ETE}}) + 2\eta_{\text{ETE}}\eta_{\text{Yb}} \quad (4)$$

The calculated results are shown in the inserted table in Figure 12f. When Yb³⁺ concentration is 2.5 mol%, the maximum theoretical QE is 164.19%.

In recent years, Eu²⁺-Yb³⁺ co-doped quantum cutting materials have received extensive attention. Sun et al.^[79] prepared an efficient broadband-sensitized NIR quantum cutting material Ca₉Y(PO₄)₇:Eu²⁺-Yb³⁺ suitable for crystalline silicon solar cells. Through the emission spectra, excitation spectra, and fluorescence lifetime, it is speculated that Eu²⁺ may transfer energy to Yb³⁺ by the CET, and Yb³⁺ emits two NIR photons at 983 nm. The QE reaches up to 179.49% when Yb³⁺ is doped with 10 mol%. In the same year, the team investigated the NIR quantum cutting effect of Eu²⁺-Yb³⁺ co-doped Sr₃Gd(PO₄)₃ phosphors.^[60] Eu²⁺ was excited by 343 nm UV light, and the NIR photons of Yb³⁺:²F_{5/2}→²F_{7/2} transition were obtained. The emission spectra and fluorescence lifetime curves of Eu²⁺ in the visible and NIR regions were measured, which confirmed the ET between Eu²⁺ and Yb³⁺. The highest ETE was 85.31% when the Yb³⁺ concentration was 30 mol%. As well Liu et al.^[85] obtained a QE of 139% in a KSrPO₄ matrix. A QE of 163.5% was achieved in borosilicate glass^[87] by Liu et al. Lin et al. achieved a QE of up to 197.4% in NaBaPO₄ and used Ag nanoparticles using the principle of localized surface plasmon resonance to accomplish an enhancement factor of quantum cutting emission intensity of 1.2337.^[24]

Table 2 summarizes the research of Eu²⁺-Yb³⁺ co-doped NIR rare-earth doped quantum cutting materials in recent years.

3.3. Ce³⁺-Nd³⁺

Nd³⁺ is also a well-reported rare-earth ion with NIR emission.^[88–92] Unlike Yb³⁺, the energy level of Nd³⁺ is very abundant, with NIR emission peaks generated by the ⁴F_{3/2}→⁴I_{9/2} (\approx 910 nm) and ⁴F_{3/2}→⁴I_{11/2} (\approx 1064) transitions before 1100 nm, at positions matching the bandgap of the silicon solar cells.^[35,93,94] Therefore, Nd³⁺ is also often used as an activator for NIR quantum cutting materials. The ET mechanism between Ce³⁺→Nd³⁺ is shown in **Figure 13**, and the ET process may exist in the following six cases: 1) Resonant nonradiative ET.

Table 2. Current status of research on Eu²⁺-Yb³⁺ co-doped NIR rare-earth doped quantum cutting materials.

Couple	Host	Preparation method	λ_{ex} [nm]	λ_{em} [nm]	ETE [%]	QE [%]	References
Eu ²⁺ -Yb ³⁺	SrAl ₂ O ₄	Solid state	370	980	73.68	147.4	[81]
	CaF ₂	Melting	320	976	51	151	[82]
	Chalcohalide glasses	Melting-quenching	395	988	85	–	[80]
	KSrPO ₄	Solid state	355	–	–	139	[85]
	Ca ₉ Y(PO ₄) ₇	Solid state	322	983	80	179	[79]
	Borate glasses	Melting	320	980	74.6	164.19	[86]
	Sr ₃ Gd(PO ₄) ₃	Solid state	343	975	85.31	–	[60]
	Borosilicate glass	Melting-quenching	400	980	74.1	163.5	[87]
	NaBaPO ₄	Solid state	355	1004	–	197.4	[24]
	Aluminosilicate Glasses	Melting-quenching	360	980	27	–	[53]
	CaAl ₂ O ₄	Solid state	325	980	55.05	–	[52]

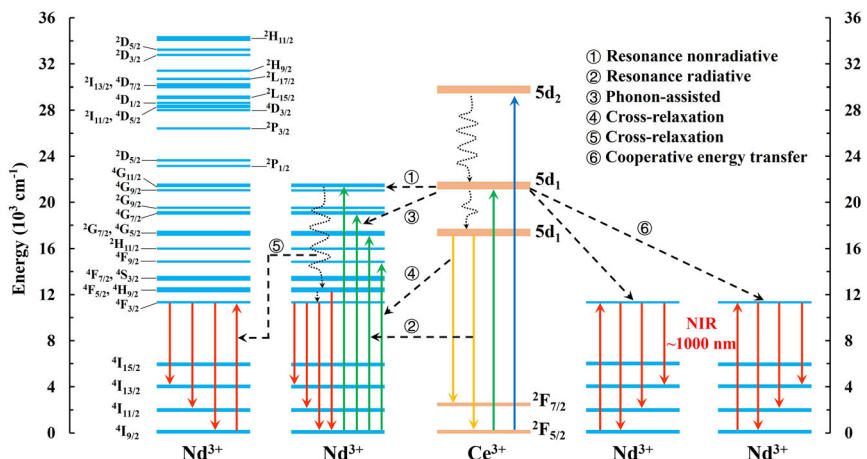


Figure 13. Schematic diagram of ET between Ce^{3+} and Nd^{3+} . ① Resonant nonradiative ET, ② resonant radiative ET, ③ phonon-assisted ET, ④ cross-relaxation between Ce^{3+} and Nd^{3+} , ⑤ cross-relaxation between Nd^{3+} and Nd^{3+} , and ⑥ CET.

Since Nd^{3+} has abundant energy levels, and there are energy levels in Nd^{3+} that match $\text{Ce}^{3+}\cdot\text{Nd}^{3+}$, Ce^{3+} may transfer energy to Nd^{3+} through resonant non-radiation; 2) Resonant radiative ET. There are energy levels in Nd^{3+} that match $\text{Ce}^{3+}\cdot\text{Nd}^{3+}$, $5d_1$, $2F_{5/2}$, and the photons emitted by $\text{Ce}^{3+}\cdot\text{Nd}^{3+}\rightarrow 2F_{5/2}$ may be absorbed by Nd^{3+} ; 3) Phonon-assisted ET. Since Nd^{3+} has abundant energy levels, and multiple energy levels in Nd^{3+} are close to the $5d_1$ of Ce^{3+} , phonon-assisted ET may occur between Ce^{3+} and Nd^{3+} with the assistance of phonons. During this process, Ce^{3+} loses part of its energy and then transfers the remaining energy to Nd^{3+} , which releases a single NIR photon; 4) Cross-relaxation between Ce^{3+} and Nd^{3+} . An energy level matching $\text{Ce}^{3+}\cdot\text{Nd}^{3+}\rightarrow 2F_{7/2}$ exists in Nd^{3+} , and the energy in Ce^{3+} may be transferred to Nd^{3+} via cross-relaxation, which emits a NIR photon when it transitions back to the ground state; 5) Cross-relaxation between Nd^{3+} and Nd^{3+} . After Ce^{3+} transfers energy to Nd^{3+} , the energy of $\text{Nd}^{3+}\cdot 4G_{11/2}\rightarrow 4F_{5/2}$, $4H_{9/2}$, $4F_{3/2}$ matches the energy of another adjacent $\text{Nd}^{3+}\cdot 4I_{9/2}\rightarrow 4F_{3/2}$, and cross-relaxation may occur. In this process, two Nd^{3+} each releases a NIR photon, realizing the two-photon emission process; and 6) CET. When Ce^{3+} is excited to the higher $5d_1$ energy level, the energy of the $\text{Ce}^{3+}\cdot\text{Nd}^{3+}\rightarrow 2F_{5/2}$ transition is about twice that of the $\text{Nd}^{3+}\cdot 4I_{9/2}\rightarrow 4F_{3/2}$, which makes the CET possible. In this process, Ce^{3+} absorbs a photon and transfers the energy to two adjacent Nd^{3+} , and then each of the two Nd^{3+} emits an NIR photon.

Tai et al.^[95] realized NIR quantum cutting in $\text{Ce}^{3+}\cdot\text{Nd}^{3+}$ co-doped YAG crystals. Figure 14a illustrates the absorption spectra of YAG: Ce^{3+} with the existence of two broadband absorption peaks assigned to $\text{Ce}^{3+}\cdot 2F_{5/2}\rightarrow 5d_1$ and $2F_{5/2}\rightarrow 5d_2$ transition. Figure 14b shows the absorption spectra of YAG: Ce^{3+} , Nd^{3+} , and several narrowband absorption peaks of Nd^{3+} are included in addition to the absorption peaks of Ce^{3+} . Figure 14c shows the excitation spectra of the YAG: Ce^{3+} samples, which have two broad peaks at 339 and 460 nm, respectively, which are still assigned to the $\text{Ce}^{3+}\cdot 2F_{5/2}\rightarrow 5d_1$, $5d_2$ transitions. In the emission spectra of Figure 14d, the peak at 531 nm is the $5d_1\rightarrow 2F_{5/2}$ transition of Ce^{3+} . As shown in Figure 14f, there is a high-intensity emission of YAG:0.01 Nd^{3+} at 1064 nm under 575 nm excitation.

Besides, the emission spectra of YAG:0.01 Ce^{3+} have a good overlap with the two sharp excitation peaks of YAG:0.01 Nd^{3+} at 530 and 575 nm (Figure 14d,e), which is favorable for the ET to occur between $\text{Ce}^{3+}\rightarrow\text{Nd}^{3+}$. Figure 14g,h display the excitation and emission spectra of YAG: $\text{Ce}^{3+}\cdot\text{Nd}^{3+}$, respectively. In the excitation spectra monitored at the 1064 nm emission of Nd^{3+} , the absorption peak of Ce^{3+} appears, evidencing the existence of the ET from Ce^{3+} to Nd^{3+} . Finally, the maximum ETE and QE were calculated to be 79.43% and 160.7%, respectively. The results indicate that $\text{Ce}^{3+}\cdot\text{Nd}^{3+}$ co-doped YAG crystals have potential applications in improving the PCE of crystalline silicon solar cells.

Zhao et al.^[96] successfully prepared $\text{Ba}_3(\text{BO}_3)_3\cdot\text{Ce}^{3+},\text{Nd}^{3+}$ NIR phosphors using the solid-phase reaction method. The Ce^{3+} ions act as an effective sensitizer to absorb the underutilized high-energy photons at 280–400 nm and convert them to NIR photons that match the silicon bandgap (850–1100 nm). In particular, the NIR emission intensity of the $\text{Ce}^{3+}\cdot\text{Nd}^{3+}$ co-doped samples was higher than that of the Nd^{3+} single-doped samples. Also, the fluorescence lifetime and the possible ET mechanism were investigated, which further confirmed the existence of the ET process between Ce^{3+} and Nd^{3+} . The highest ETE of 50.5% was achieved when the Nd^{3+} doping amount was 0.055.

Chen et al.^[62] synthesized $\text{Ce}^{3+}\cdot\text{Nd}^{3+}$ co-doped $(\text{Sr}_{0.6}\text{Ca}_{0.4})_3(\text{Al}_{0.6}\text{Si}_{0.4})\text{O}_{4.4}\text{F}_{0.6}$ phosphors using the solid-state method. The absorption and fluorescence spectra are shown in Figure 14i–k. In Figure 14i, for the single-doped Ce^{3+} or $\text{Ce}^{3+}\cdot\text{Nd}^{3+}$ co-doped samples, there are two absorption peaks in the range of 330–450 nm caused by the $f\text{-}d$ transition of Ce^{3+} ions. For the single-doped Nd^{3+} or $\text{Ce}^{3+}\cdot\text{Nd}^{3+}$ co-doped samples, two absorption peaks appeared at 500–620 nm, which were attributed to the absorption of Nd^{3+} ions. As seen in Figure 14j, for the $\text{Ce}^{3+}\cdot\text{Nd}^{3+}$ co-doped sample monitored at 1093 nm, the excitation peak at 440 nm is attributed to Ce^{3+} and the two subpeaks at 535 and 593 nm are attributed to Nd^{3+} , consistent with the absorption spectra. The excitation spectra of Nd^{3+} doped samples can also confirm this determination

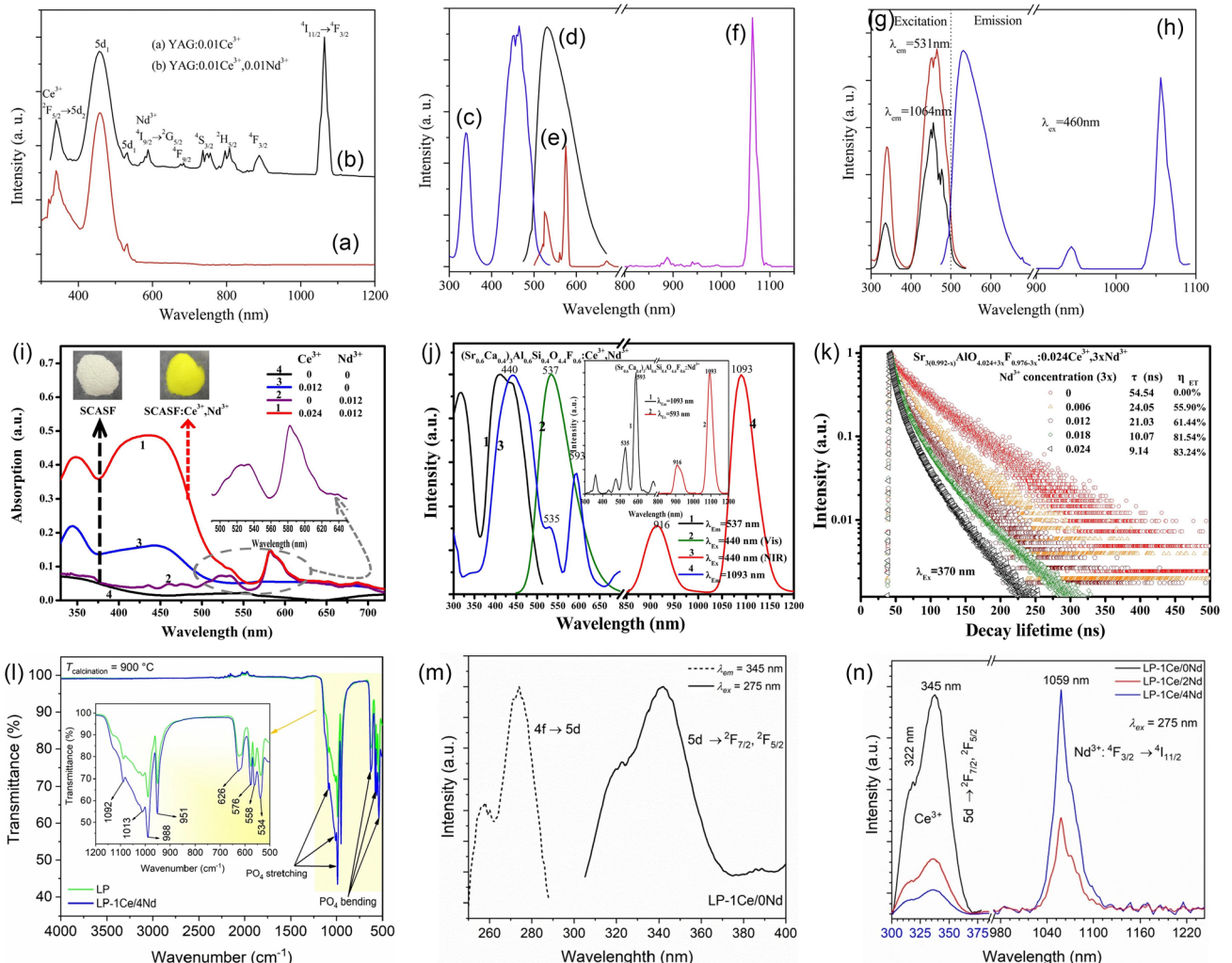


Figure 14. Absorption spectra of a) YAG:Ce³⁺ and b) YAG:Ce³⁺, Nd³⁺, c) excitation ($\lambda_{\text{em}} = 531 \text{ nm}$) and d) emission ($\lambda_{\text{ex}} = 460 \text{ nm}$) spectra of YAG:Ce³⁺, e) excitation ($\lambda_{\text{em}} = 1064 \text{ nm}$) and f) emission ($\lambda_{\text{ex}} = 575 \text{ nm}$) spectra of YAG:Nd³⁺, g) excitation ($\lambda_{\text{em}} = 531 \text{ and } 1064 \text{ nm}$) and h) emission ($\lambda_{\text{ex}} = 460 \text{ nm}$) spectra of YAG: Ce³⁺, Nd³⁺. Reproduced with permission.^[95] Copyright 2015, Elsevier. i) Absorption spectra of different doping amounts. j) excitation (black) and emission (green) spectra in the visible region for the sample singly doped with Ce³⁺ and excitation (blue) and emission (red) spectra in the NIR region for the sample co-doped with Ce³⁺-Nd³⁺, and k) luminescence decay curves of (Sr_{0.592-x}Ca_x)₃(Al_{0.6}Si_{0.4})O_{4.424+3x}F_{0.576-3x}:0.024Ce³⁺, 3xNd³⁺. Reproduced with permission.^[62] Copyright 2015, The American Ceramic Society. l) FTIR spectra of LaPO₄ (LP) and LaPO₄ (LP):Ce/Nd samples, m) excitation (dotted line) and emission (dark line) spectra of LaPO₄:Ce³⁺, and n) emission spectra of LaPO₄:Ce³⁺, xNd³⁺ samples at 275 nm excitation. Reproduced with permission.^[97] Copyright 2022, Springer Nature.

(the inset of Figure 14j). Additionally, the ET process Ce³⁺→Nd³⁺ was confirmed by testing the fluorescence decay curve of Ce³⁺-Nd³⁺ co-doped samples, and the ETE reached the maximum of 83.24% when the Nd³⁺ concentration was 0.024 (Figure 14k).

AitMellal et al.^[97] synthesized Ce³⁺-Nd³⁺ co-doped LaPO₄ phosphors using a co-precipitation method. They investigated the fundamental vibrational modes of the undoped and Ce³⁺-Nd³⁺ co-doped samples employing FTIR (Fourier transform infrared spectroscopy) (Figure 14l). The two spectra show similar characteristics, which suggests that doping hardly affects the vibrational modes of the matrix materials. The LaPO₄:Ce³⁺, Nd³⁺ phosphors were studied using excitation spectra and emission spectra (Figure 14m,n). Under 275 nm excitation, LaPO₄:

Ce³⁺,Nd³⁺ may emit 1059 nm NIR photons, which was thought as the result of the cross-relaxation and CET. However, on the basis of the above discussion, it is known that resonance and phonon-assisted ET may also occur between Ce³⁺-Nd³⁺.

Table 3 summarizes the research of Ce³⁺-Nd³⁺ co-doped NIR rare-earth doped quantum cutting materials in recent years.

3.4. Eu²⁺-Nd³⁺

Since Eu²⁺ has a broad emission band and Nd³⁺ has abundant energy levels, the ET mechanism between Eu²⁺→Nd³⁺ is more complicated, and the possible ET mechanisms are shown in Figure 15: 1) Resonant nonradiative ET. Since Nd³⁺ has

Table 3. Current status of research on Ce^{3+} - Nd^{3+} co-doped NIR rare-earth doped quantum cutting materials.

Couple	Host	Preparation method	λ_{ex} [nm]	λ_{em} [nm]	ETE (%)	QE (%)	References
Ce^{3+} - Nd^{3+}	YAG	Solid state	460	1064	79.43	160.7	[95]
	$\text{Ba}_3\text{Y}(\text{BO}_3)_3$	Solid state	356	1059	50.5	—	[96]
	SCASF	Solid state	440	1093	83.24	—	[62]
	LaPO_4	Co-precipitation	275	1059	72	172	[97]

abundant energy levels, and there are energy levels in Nd^{3+} that match $\text{Eu}^{2+}:5d_1$, Eu^{2+} may transfer energy to Nd^{3+} through resonant non-radiation; 2) Resonant radiative ET. The photons emitted by $\text{Eu}^{2+}:4f^65d^1 \rightarrow 4f^7$ may be absorbed by Nd^{3+} ; 3) Phonon-assisted ET. Since Nd^{3+} has abundant energy levels, and there are multiple energy levels in Nd^{3+} that are similar to $\text{Eu}^{2+}:4f^65d^1$, phonon-assisted ET may occur between Eu^{2+} and Nd^{3+} with the assistance of phonons; 4) Cross-relaxation between two Nd^{3+} ions. After Eu^{2+} transfers energy to Nd^{3+} , the energy of $\text{Nd}^{3+}:4G_{11/2} \rightarrow 4F_{5/2}$, $4H_{9/2}$, $4F_{3/2}$ matches the energy of another adjacent $\text{Nd}^{3+}:4I_{9/2} \rightarrow 4F_{3/2}$, and cross-relaxation may occur. In this process, two Nd^{3+} each releases a NIR photon, realizing the two-photon emission process; and 5) CET. The transition energy of $\text{Eu}^{2+}:4f^65d^1 \rightarrow 4f^7$ is close to twice that of $\text{Nd}^{3+}:4I_{9/2} \rightarrow 4F_{3/2}$. Therefore, Eu^{2+} may transfer energy to two nearby Nd^{3+} through CET, and each of the two Nd^{3+} emits an NIR photon.

Compared with the double-peak excitation of Ce^{3+} , Eu^{2+} is a single-peak with broader excitation spectra and a higher photon utilization efficiency. Moreover, Yb^{3+} has only two energy levels, $^2F_{7/2}$ and $^2F_{5/2}$, and the energy level difference between them corresponds to an absorption wavelength of about 980 nm, which cannot absorb photon energy in the UV-visible region. Compared with Yb^{3+} , Nd^{3+} has abundant energy levels and multiple absorption peaks between 450–900 nm, which overlaps well with the emission spectra of Eu^{2+} , facilitating the ET between Eu^{2+} - Nd^{3+} . In addition, Nd^{3+} has NIR emission peaks generated by $4F_{3/2} \rightarrow 4I_{9/2}$ (≈ 910 nm) and $4F_{3/2} \rightarrow 4I_{11/2}$ (≈ 1064) transitions

before 1100 nm, which better match the bandgap of the silicon solar cells. Therefore, Eu^{2+} - Nd^{3+} co-doped quantum cutting materials have attracted much attention among many rare-earth ion pairs. The most common matrix materials for preparing Eu^{2+} - Nd^{3+} co-doped quantum cutting materials are oxides, silicates, borates, phosphates, and aluminates. Researchers have made many attempts in various matrix materials to prepare quantum cutting materials with excellent performance.

Talewar et al.^[98] successfully prepared a highly efficient NIR luminescent material $\text{Sr}_5(\text{PO}_4)_3\text{Cl}:\text{Eu}^{2+},\text{Nd}^{3+}$ (Figure 16a). In Figure 16d, the NIR emission peaks of Nd^{3+} were observed at 905, 1060, and 1335 nm for the Eu^{2+} - Nd^{3+} co-doped phosphors under 370 nm excitation. Compared with the single-doped Nd^{3+} sample (Figure 16e), the emission of the Eu^{2+} - Nd^{3+} co-doped phosphors is stronger and demonstrates that the Eu^{2+} ion is an effective sensitizer, which absorbs photons in the range of 220–440 nm and then transfers the energy to Nd^{3+} ions for producing strong NIR emission in the range of 850–1400 nm. As shown in Figure 16f–i, $\text{Sr}_5(\text{PO}_4)_3\text{Cl}:\text{Eu}^{2+},\text{Nd}^{3+}$ phosphors have broad excitation spectra in the UV-blue region and strong NIR emission spectra, and the emission band of Nd^{3+} matches the spectral response of silicon cells, which has potential applications in silicon solar cells.

Tai et al.^[99] investigated the quantum cutting process between Eu^{2+} and Nd^{3+} in $\text{SrAl}_2\text{O}_4:\text{Eu}^{2+},\text{Nd}^{3+}$. As seen in Figure 16j–m, both the excitation and emission spectra of $\text{SrAl}_2\text{O}_4:\text{Eu}^{2+}$ exhibit typical broad bands. $\text{SrAl}_2\text{O}_4:\text{Nd}^{3+}$ has a strong emission at 1064 nm, which matches the bandgap of the silicon solar cells.

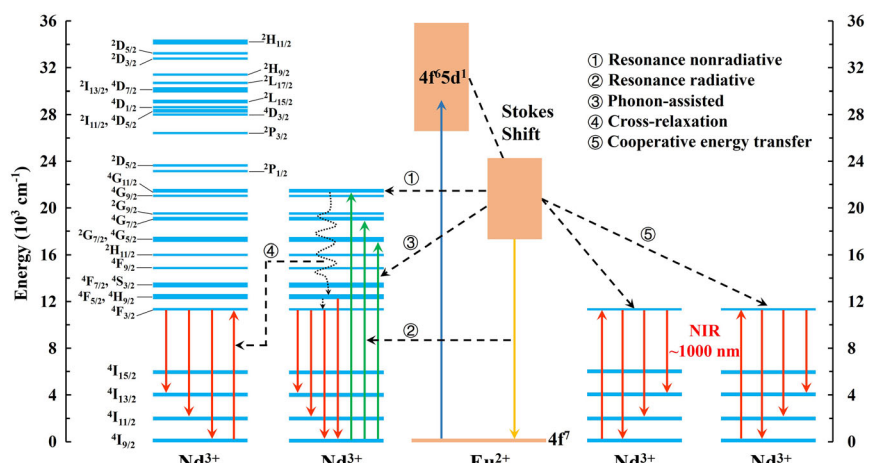


Figure 15. Schematic diagram of ET between Eu^{2+} and Nd^{3+} . ① Resonance nonradiative ET, ② resonant radiative ET, ③ phonon-assisted ET, ④ cross-relaxation between two Nd^{3+} ions, and ⑤ CET.

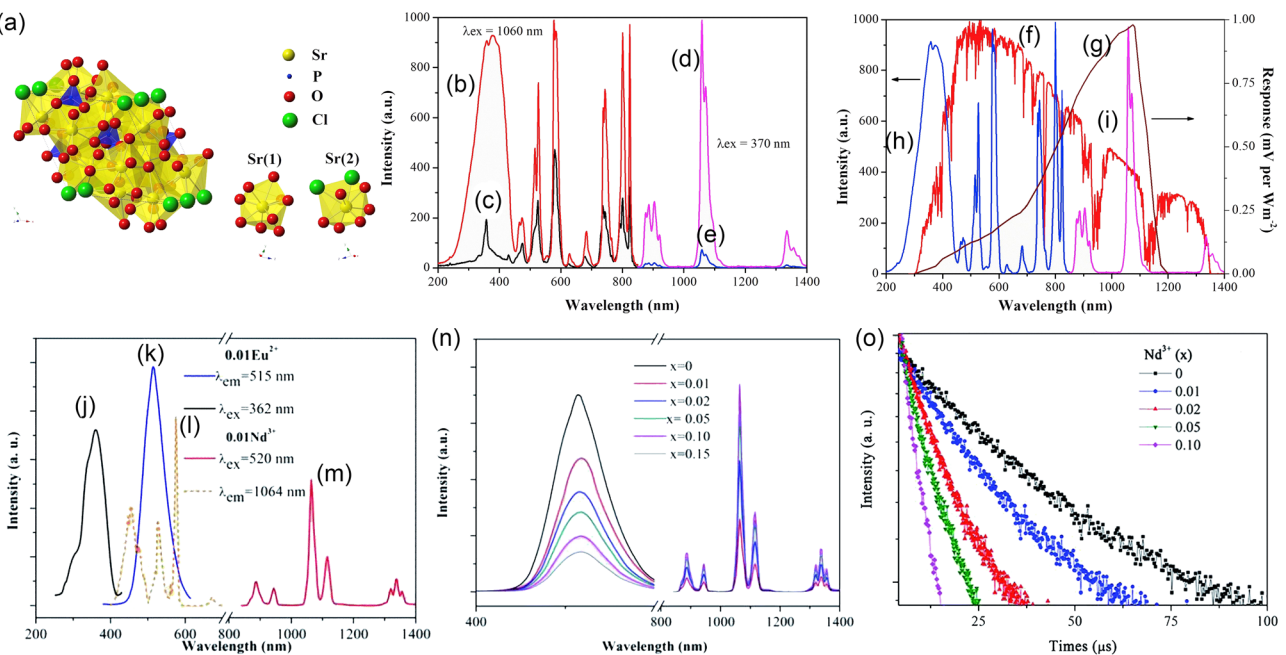


Figure 16. a) Crystal structure of $\text{Sr}_5(\text{PO}_4)_3\text{Cl}$ phosphor, b) excitation and d) emission spectra of the $\text{Sr}_5(\text{PO}_4)_3\text{Cl}:\text{Eu}^{2+}, \text{Nd}^{3+}$, c) excitation and e) emission spectra of the $\text{Sr}_5(\text{PO}_4)_3\text{Cl}:\text{Nd}^{3+}$. f) AM1.5 solar spectrum. g) Spectral response of crystalline Silicon solar cell. h) Excitation and i) emission spectra of $\text{Sr}_5(\text{PO}_4)_3\text{Cl}:\text{Eu}^{2+}, \text{Nd}^{3+}$. Reproduced with permission.^[98] Copyright 2020, Elsevier. j) Excitation and k) emission spectra of $\text{SrAl}_2\text{O}_4:0.01\text{Eu}^{2+}$. l) Excitation and m) emission spectra of $\text{SrAl}_2\text{O}_4:0.01\text{Nd}^{3+}$. n) Emission spectra of $\text{SrAl}_2\text{O}_4:0.01\text{Eu}^{2+}, x\text{Nd}^{3+}$ ($\lambda_{\text{ex}} = 362 \text{ nm}$). o) Luminescence decay curves of Eu^{2+} at 515 nm emission under 362 nm excitation. Reproduced with permission.^[99] Copyright 2018, The Royal Society of Chemistry.

Furthermore, it can be noticed that the emission spectra of Eu^{2+} and the excitation spectra of Nd^{3+} have a superior spectral overlap, which is favorable for the ET between Eu^{2+} and Nd^{3+} . Figure 16n shows the concentration-dependent emission spectra under 362 nm ($\text{Eu}^{2+}: 4f^7 \rightarrow 4F^6 5d^1$) excitation. As the Nd^{3+} concentration increases, it is observed that the Eu^{2+} emission intensity decreases gradually, which is related to the ET from Eu^{2+} to Nd^{3+} . When the concentration of Nd^{3+} was greater than 0.10, the concentration quenching occurred between Nd^{3+} ions. Finally, the theoretical maximum QE of 177.1% was calculated using the decay lifetime curve of Figure 16o.

Tumram et al.^[100] reported the NIR emission of $\text{KCl} \cdot \text{SrCl}_2: \text{Eu}^{2+}, \text{Nd}^{3+}$ phosphors excited by near-UV light, and demonstrated that the NIR emission is the result of the ET from $\text{Eu}^{2+} \rightarrow \text{Nd}^{3+}$ with an ETE as high as 87%. The phosphors can be used to convert the near-UV emission in the solar spectra to the NIR region around 1000 nm, which will help prevent the degradation of the crystalline silicon solar cells from

long-term exposure to UV radiation. Moreover, it can effectively utilize the near-UV region to improve the PCE of the solar cells.

Tawalare et al.^[101] synthesized strong NIR emission phosphors $\text{Ca}_5(\text{PO}_4)_3\text{Cl}:\text{Eu}^{2+}, \text{Nd}^{3+}$ and characterized them by X-ray diffraction, reflection spectra, excitation spectra, and emission spectra, as well as fluorescence lifetime. Due to the ET of $\text{Eu}^{2+} \rightarrow \text{Nd}^{3+}$, the broadband absorption in the near-UV band can excite the phosphors to emit NIR light at 1069 nm, and the ETE of $\text{Eu}^{2+} \rightarrow \text{Nd}^{3+}$ is as high as 80.8%.

Vyas et al.^[102] reported the NIR luminescence of $\text{Ba}_2\text{SiO}_4: \text{Eu}^{2+}, \text{Nd}^{3+}$, and observed efficient ET between $\text{Eu}^{2+} \rightarrow \text{Nd}^{3+}$ with the ETE close to 80%. This ET allows near-UV-violet light near 350–450 nm to be converted to NIR light around 1067 nm, and the phosphors have great application potential as a solar spectrum modulator.

Table 4 summarizes the research of $\text{Eu}^{2+}-\text{Nd}^{3+}$ co-doped NIR rare-earth doped quantum cutting materials in recent years.

Table 4. Current status of research on $\text{Eu}^{2+}-\text{Nd}^{3+}$ co-doped NIR rare-earth doped quantum cutting materials.

Couple	Host	Preparation method	λ_{ex} [nm]	λ_{em} [nm]	ETE [%]	QE [%]	References
$\text{Eu}^{2+}-\text{Nd}^{3+}$	$\text{Sr}_5(\text{PO}_4)_3\text{Cl}$	Solid state	370	1060	29	–	[98]
	SrAl_2O_4	Solid state	362	1064	77.1	177.1	[99]
	$\text{KCl} \cdot \text{SrCl}_2$	Co-precipitation	400	1065	87	–	[100]
	$\text{Ca}_5(\text{PO}_4)_3\text{Cl}$	Solid state	400	1069	80.8	–	[101]
	Ba_2SiO_4	Solid state	400	1067	78.9	–	[102]

4. Summary and Perspective

Broadband-sensitized NIR quantum cutting materials for silicon solar cells have been reviewed. Quantum cutting materials can theoretically break through the Shockley–Queisser limit, and the bands of the emission spectra are easily adjustable and have high luminescence intensity and QE, which have broad application prospects. They are mainly glass and glass ceramics with rare-earth ions such as Ce^{3+} and Eu^{2+} as sensitizers, whose emission can be adjusted to match the wavelength bands of different solar cells. The broadband-sensitized NIR quantum cutting materials are usually co-doped with $\text{Ce}^{3+}/\text{Eu}^{2+}$ and Yb^{3+} , achieving the luminescence of Yb^{3+} around 1000 nm by the ET between the rare-earth ions, thereby improving the efficiency of the crystalline silicon solar cells. Besides Yb^{3+} , Nd^{3+} can also have NIR emission at 1064 nm, which matches the bandgap of the silicon solar cells. However, the conversion efficiency of the silicon solar cells with the quantum cutting materials is far from the limit efficiency of 38.6% predicted by Turpe's theory. The focus and difficulty of current research are how to further improve the performance of the quantum cutting materials so that they can be applied. The following lists some of the issues and directions of the exploration that the authors consider important for the reader's reference: 1) In-depth study of the ET mechanism. Quantum cutting luminescence is based on the ET process between the rare-earth ions, which is a complex process with the ET between different matrix materials and different ions and is also influenced by many factors, such as temperature, light, concentration, etc. The in-depth study of the ET mechanism provides the theoretical basis for preparing quantum cutting materials with high QE; 2) How to improve the absorption of high-energy photons. Finding new quantum cutting materials with large absorption cross-sections in the high-energy sunlight region (300–500 nm), such as ions or matrixes with broad-spectra absorption, will be the focus of future research; 3) How to reduce concentration quenching. Doping more Yb^{3+} ions and Nd^{3+} ions can cause concentration quenching, seriously affecting the practical application of NIR quantum cutting materials; 4) How to test precisely QE. Due to the nonradiative energy loss, the actual QE should be smaller than the theoretically calculated value. In the existing methods, the fluorescence spectrum is used to calculate QE. However, the measured data of the detectors for different wavelengths are different and cannot be directly compared, which leads to inaccurate results; 5) Nitride luminescent materials doped with rare-earth ions are widely used in LED lighting, displays, fluorescent markers, etc., due to their broad absorption spectra (the absorption range covers UV-blue-green), high luminous efficiency, high stability, non-toxicity, and other advantages. For example, $\text{CaAlSiN}_3:\text{Eu}^{2+}$, $\text{BaAlSiN}_3:\text{Eu}^{2+}$, $\text{SrAlSiN}_3:\text{Ce}^{3+}$, and other commercial phosphors. These materials are suitable as matrices for broadband-sensitized near-infrared quantum cutting materials due to their excellent optical properties. However, there are few research reports in this area, and a great deal of effort is needed to develop efficient nitride-based near-infrared quantum cutting materials to improve the efficiency of crystalline silicon solar cells; and 6) The packaging process of the solar cells. The surface reflectivity of the solar cells is an essential factor affecting PCE. Although some packaging processes that can improve the performance of the cells have been proposed, the

coating materials and fabrication costs are relatively high and only suitable for use in laboratories. Based on the proven feasibility of the principle, it is meaningful to develop packaging processes that can apply quantum cutting materials to the mass production of solar cells or modules.

Acknowledgements

This work was supported by the Primary Research & Development Plan of Jiangsu Province (grant no. BE2016175).

Conflict of Interest

The authors declare no conflict of interest.

Keywords

broadband sensitized, near-infrared phosphors, quantum cutting, rare-earth luminescence, silicon solar cells

Received: January 10, 2024

Revised: February 9, 2024

Published online: February 22, 2024

- [1] Y. X. Ji, W. X. Chen, D. Yan, J. Bullock, Y. Xu, Z. H. Su, W. T. Yang, J. S. Laird, T. Zheng, N. Wu, W. S. Zha, Q. Luo, C. Q. Ma, T. A. Smith, F. Y. Liu, P. Mulvaney, *Small* **2023**, *20*, 2307242.
- [2] S. R. Wang, C. Wu, H. H. Yao, L. M. Ding, F. Hao, *Mater. Chem. Front.* **2023**, *7*, 789.
- [3] Y. L. Li, Z. Ma, S. Y. Hou, Q. Y. Liu, G. Y. Yan, X. S. Li, T. J. Yu, Z. W. Du, J. B. Yang, Y. Chen, W. You, Q. Yang, Y. Xiang, S. F. Tang, X. L. Yue, M. Zhang, W. F. Zhang, J. Yu, Y. L. Huang, J. L. Xie, C. Tang, Y. H. Mai, K. Sun, *J. Mater. Sci. Technol.* **2024**, *176*, 236.
- [4] X. Z. Chen, Q. Luo, C. Q. Ma, *Chin. J. Polym. Sci.* **2023**, *41*, 1169.
- [5] M. A. Aditama, M. N. Al Faris, P. Sambegoro, *Sol. Energy* **2023**, *266*, 112156.
- [6] K. Aitola, G. G. Sonai, M. Markkanen, J. J. Kaschuk, X. L. Hou, K. Miettunen, P. D. Lund, *Sol. Energy* **2022**, *237*, 264.
- [7] J. Puustinen, J. Hilska, A. Aho, E. Luna, A. Fihlman, M. Guina, *Sol. Energy Mater. Sol. C* **2024**, *264*, 112598.
- [8] J. A. Röhr, B. E. Sartor, J. Lipton, A. D. Taylor, *Nat. Photonics* **2023**, *17*, 747.
- [9] S. Moon, K. Kim, Y. Kim, H. K. Kang, K. H. Park, J. J. Lee, *Sol. RRL* **2023**, *7*, 2300387.
- [10] W. H. Wang, X. Liu, J. C. Wang, C. Chen, J. S. Yu, D. W. Zhao, W. H. Tang, *Adv. Energy Mater.* **2023**, *13*, 2370088.
- [11] S. Z. Wang, T. Xie, R. Liang, Y. Zhang, F. J. Ma, D. Payne, G. Scardera, B. Hoex, *ACS Appl. Nano Mater.* **2022**, *5*, 11636.
- [12] T. Matsui, H. Sai, A. Bidiville, H. J. Hsu, K. Matsubara, *Sol. Energy* **2018**, *170*, 486.
- [13] Z. S. Yu, M. Leilaeioun, Z. Holman, *Nat. Energy* **2016**, *1*, 16137.
- [14] L. L. Yan, C. Han, B. Shi, Y. Zhao, X. D. Zhang, *Mater. Today Nano* **2019**, *7*, 100045.
- [15] M. A. Green, *Nat. Energy* **2023**, *8*, 783.
- [16] Z. Q. Sun, X. Q. Chen, Y. C. He, J. J. Li, J. Q. Wang, H. Yan, Y. Z. Zhang, *Adv. Energy Mater.* **2022**, *12*, 2270094.
- [17] W. Shockley, H. J. Queisser, *J. Appl. Phys.* **1961**, *32*, 510.

- [18] H. Lin, M. Yang, X. N. Ru, G. S. Wang, S. Yin, F. G. Peng, C. J. Hong, M. H. Qu, J. X. Lu, L. Fang, C. Han, P. Procel, O. Isabella, P. Q. Gao, Z. G. Li, X. X. Xu, *Nat. Energy* **2023**, *8*, 789.
- [19] B. Zhou, X. H. Yin, J. L. Zhang, G. G. Zeng, B. Li, J. Q. Zhang, L. H. Feng, *Opt. Mater.* **2020**, *110*, 110505.
- [20] U. Y. Won, T. H. Ly, Y. R. Kim, W. T. Kang, Y. S. Shin, K. Y. Lee, J. S. Heo, K. N. Kim, Y. H. Lee, W. J. Yu, *Nano Energy* **2018**, *53*, 398.
- [21] E. López, A. Martí, E. Antolín, A. Luque, *Energies* **2020**, *13*, 3044.
- [22] D. Wu, X. L. Dong, W. G. Xiao, Z. D. Hao, J. H. Zhang, *Inorg. Chem.* **2019**, *58*, 234.
- [23] J. Li, L. Chen, Z. D. Hao, X. Zhang, L. G. Zhang, Y. S. Luo, J. H. Zhang, *Inorg. Chem.* **2015**, *54*, 4806.
- [24] L. Lin, J. X. Chen, Z. Z. Wang, Z. H. Feng, F. Huang, B. Zheng, L. L. Huang, Z. P. Yu, Z. Q. Zheng, *Mater. Res. Bull.* **2017**, *93*, 35.
- [25] H. Y. Wang, S. Ye, S. Li, T. H. Liu, J. Lin, D. P. Wang, *J. Alloy Compd.* **2015**, *648*, 13.
- [26] B. S. Richards, *Sol. Energy Mater. Sol. C* **2006**, *90*, 2329.
- [27] P. Babu, I. R. Martín, V. Lavín, U. R. Rodríguez-Mendoza, H. J. Seo, K. V. Krishanaiah, V. Venkatramu, *J. Lumin.* **2020**, *226*, 117424.
- [28] Q. Wang, J. B. Qiu, Z. G. Song, Z. W. Yang, Z. Y. Yin, D. C. Zhou, S. Q. Wang, *Opt. Mater.* **2016**, *54*, 229.
- [29] Z. H. Zou, L. Feng, C. Cao, J. C. Zhang, Y. H. Wang, *Sci Rep* **2016**, *6*, 24884.
- [30] S. W. Li, J. Y. Gao, C. Guan, J. Y. Yue, *Ferroelectrics* **2022**, *596*, 107.
- [31] L. Oulmaati, S. El Amrani, K. Bouziane, A. Bouajaj, M. R. Britel, F. Enrichi, M. Ferrari, *Appl. Sci.* **2023**, *13*, 9390.
- [32] T. Trupke, M. A. Green, P. Würfel, *J. Appl. Phys.* **2002**, *92*, 1668.
- [33] K. M. Deng, T. Gong, L. X. Hu, X. T. Wei, Y. H. Chen, M. Yin, *Opt. Express* **2011**, *19*, 1749.
- [34] W. Shao, C. K. Lim, Q. Li, M. T. Swihart, P. N. Prasad, *Nano Lett.* **2018**, *18*, 4922.
- [35] J. M. Li, S. A. Zhang, H. M. Luo, Z. F. Mu, Z. Z. Li, Q. P. Du, J. Q. Feng, F. G. Wu, *Opt. Mater.* **2018**, *85*, 523.
- [36] R. T. Wegh, H. Donker, E. V. D. van Loef, K. D. Oskam, A. Meijerink, *J. Lumin.* **2000**, *87–89*, 1017.
- [37] S. M. Ferro, M. Wobben, B. Ehrler, *Mater. Horiz.* **2021**, *8*, 1072.
- [38] X. B. Chen, G. J. Yang, Y. Z. Zhang, Z. W. Deng, L. L. Hu, S. Li, C. L. Yu, Z. J. Chen, J. S. Cui, X. D. Chen, H. Y. Zhou, Z. L. Wu, *Spectrosc. Spectr. Anal.* **2012**, *32*, 2597.
- [39] G. H. Dieke, H. M. Crosswhite, H. Crosswhite, in *Spectra and Energy Levels of Rare Earth Ions in Crystals*, Interscience Publishers, New York **1968**.
- [40] F. Auzel, *Chem. Rev.* **2004**, *104*, 139.
- [41] D. L. Dexter, *Phys. Rev.* **1957**, *108*, 630.
- [42] W. W. Piper, J. A. DeLuca, F. S. Ham, *J. Lumin.* **1974**, *8*, 344.
- [43] J. L. Sommerdijk, A. Bril, A. W. de Jager, *J. Lumin.* **1974**, *8*, 341.
- [44] R. T. Wegh, H. Donker, K. D. Oskam, A. Meijerink, *Science* **1999**, *283*, 663.
- [45] D. C. Li, G. P. Zhu, *Materials* **2022**, *15*, 5282.
- [46] M. R. M. de Sousa, T. O. Sales, W. Q. Santos, W. F. Silva, C. Jacinto, *J. Lumin.* **2021**, *233*, 117919.
- [47] D. Y. Shi, S. B. Lin, X. X. Zhao, A. L. Feng, Q. Xu, *Results Phys.* **2020**, *19*, 103411.
- [48] S. Q. Luo, L. J. Zhao, N. Hu, M. Zhang, P. Zhang, Y. Z. Wang, H. Yu, *Chin. Phys. Lett.* **2011**, *28*, 034207.
- [49] N. S. Sawala, P. R. Somani, S. K. Omanwar, *J. Mater. Sci.* **2017**, *28*, 142.
- [50] Y. Y. Hao, Y. Wang, X. Y. Hu, X. X. Liu, E. Z. Liu, J. Fan, H. Miao, Q. Sun, *Ceram. Int.* **2016**, *42*, 9396.
- [51] J. D. Chen, H. Zhang, F. Li, H. Guo, *Mater. Chem. Phys.* **2011**, *128*, 191.
- [52] Y. Teng, J. J. Zhou, S. Ye, J. R. Qiu, *J. Electrochem. Soc.* **2010**, *157*, A1073.
- [53] J. J. Zhou, Y. Teng, G. Lin, X. Q. Xu, Z. J. Ma, J. R. Qiu, *J. Electrochem. Soc.* **2010**, *157*, B1146.
- [54] H. Zhang, J. D. Chen, H. Guo, *J. Rare Earth* **2011**, *29*, 822.
- [55] A. A. Pathak, R. A. Talewar, C. P. Joshi, S. V. Moharil, *J. Lumin.* **2016**, *179*, 350.
- [56] G. J. Shao, C. G. Lou, D. Xiao, *J. Lumin.* **2015**, *157*, 344.
- [57] X. F. Liu, Y. Teng, Y. X. Zhuang, J. H. Xie, Y. B. Qiao, G. P. Dong, D. P. Chen, J. R. Qiu, *Opt. Lett.* **2009**, *34*, 3565.
- [58] J. Y. Sun, G. C. Sun, Y. N. Sun, L. Han, *Opt. Mater.* **2014**, *36*, 1097.
- [59] L. G. Wang, Y. F. Li, Z. Wang, R. Yang, Y. Y. Tong, L. L. Sun, *J. Lumin.* **2018**, *203*, 121.
- [60] J. Y. Sun, Y. N. Sun, J. H. Zeng, H. Y. Du, *Opt. Mater.* **2013**, *35*, 1276.
- [61] J. Li, J. Zhang, X. Zhang, Z. Hao, Y. Luo, *J. Alloy Compd.* **2014**, *583*, 96.
- [62] J. J. Chen, J. Liu, H. M. Yin, S. L. Jiang, H. Yao, X. B. Yu, *J. Am. Ceram. Soc.* **2016**, *99*, 141.
- [63] W. N. Xu, Q. Q. Yan, J. Ren, G. R. Chen, *J. Lumin.* **2013**, *134*, 75.
- [64] W. L. Zhou, J. Yang, J. Wang, Y. Li, X. J. Kuang, J. K. Tang, H. B. Liang, *Opt. Express* **2012**, *20*, A510.
- [65] Y. P. Tai, X. Z. Li, X. G. Du, B. L. Pan, G. H. Yuan, *RSC Adv.* **2018**, *8*, 23268.
- [66] K. Yue, Z. You, P. Ke, J. X. Wen, M. Jia, T. Y. Wang, *Opt. Mater. Express* **2022**, *12*, 653.
- [67] D. Q. Chen, Y. S. Wang, Y. L. Yu, P. Huang, F. Y. Weng, *J. Appl. Phys.* **2008**, *104*, 116105.
- [68] X. X. Liu, X. Y. Hu, H. Miao, G. W. Zhang, J. L. Mu, T. X. Han, D. K. Zhang, *Sol. Energy* **2016**, *134*, 45.
- [69] D. L. Zhou, R. Sun, W. Xu, N. Ding, D. Y. Li, X. Chen, G. C. Pan, X. Baio, H. W. Song, *Nano Lett.* **2019**, *19*, 6904.
- [70] L. Li, C. G. Lou, H. H. Cao, H. Diao, S. K. Karunakaran, *Appl. Phys. Lett.* **2018**, *113*, 101905.
- [71] L. Li, C. G. Lou, X. L. Sun, Y. F. Xie, L. Hu, K. S. Kumar, *ECS J. Solid State Sci. Technol.* **2016**, *5*, R146.
- [72] F. Y. Fan, F. Liu, S. S. Yu, J. X. Wu, J. Zhang, T. L. Wang, Y. Y. Li, L. Zhao, Q. P. Qiang, W. B. Chen, *J. Lumin.* **2022**, *241*, 118511.
- [73] T. Y. Sun, X. Chen, L. M. Jin, H. W. Li, B. Chen, B. Fan, B. Moine, X. S. Qiao, X. P. Fan, S. W. Tsang, S. F. Yu, F. Wang, *J. Phys. Chem. Lett.* **2017**, *8*, 5099.
- [74] K. S. Kumar, C. G. Lou, A. G. Manohari, C. Huihui, D. Pribat, *RSC Adv.* **2017**, *7*, 24674.
- [75] W. B. Dai, J. Zhou, K. Huang, J. Hu, S. Xu, M. Xu, *J. Alloy Compd.* **2019**, *786*, 662.
- [76] C. L. Han, L. Luo, G. S. Dong, W. Zhang, Y. H. Wang, *Mater. Res. Bull.* **2017**, *96*, 286.
- [77] S. K. Karunakaran, C. G. Lou, G. M. Arumugam, H. H. Cao, D. Pribat, *Sol. Energy* **2019**, *188*, 45.
- [78] C. M. Zhang, L. J. Wang, X. Ji, Y. X. Pin, P. F. Zhu, G. S. Li, *Optik* **2018**, *171*, 308.
- [79] J. Y. Sun, W. Zhou, Y. N. Sun, J. H. Zeng, *Opt. Commun.* **2013**, *296*, 84.
- [80] Q. Q. Yan, J. Ren, Y. Tong, G. R. Chen, *J. Am. Ceram. Soc.* **2013**, *96*, 1349.
- [81] Y. P. Tai, G. J. Zheng, H. Wang, J. T. Bai, *J. Solid State Chem.* **2015**, *226*, 250.
- [82] H. Lin, D. Q. Chen, Y. L. Yu, Z. F. Shan, P. Huang, A. P. Yang, Y. S. Wang, *J. Alloy Compd.* **2011**, *509*, 3363.
- [83] X. L. Liang, Z. W. Xing, Y. X. Yang, S. F. Wang, G. R. Chen, *J. Am. Ceram. Soc.* **2011**, *94*, 849.
- [84] W. J. Yang, L. Y. Luo, T. M. Chen, N. S. Wang, *Chem. Mater.* **2005**, *17*, 3883.
- [85] T. C. Liu, G. G. Zhang, X. B. Qiao, J. Wang, H. J. Seo, D. P. Tsai, R. S. Liu, *Inorg. Chem.* **2013**, *52*, 7352.
- [86] J. J. Zhou, Y. X. Zhuang, S. Ye, Y. Teng, G. Lin, B. Zhu, J. H. Xie, J. R. Qiu, *Appl. Phys. Lett.* **2009**, *95*, 141101.

- [87] Z. J. Liu, N. L. Dai, L. Y. Yang, J. Y. Li, *Appl. Phys. A: Mater. Sci. Process.* **2015**, *119*, 553.
- [88] T. Zhezhera, P. Gluchowski, M. Nowicki, M. Chrunik, A. Majchrowski, K. M. Kosyl, D. Kasprowicz, *J. Mater. Sci.* **2022**, *57*, 185.
- [89] S. Xu, W. Xu, Y. S. Zhu, B. A. Dong, X. Bai, L. Xu, H. W. Song, *J. Appl. Phys.* **2013**, *113*, 073101.
- [90] J. Y. Sun, Y. N. Sun, C. Cao, Z. G. Xia, H. Y. Du, *Appl. Phys. B: Lasers Opt.* **2013**, *111*, 367.
- [91] H. K. Dan, T. D. Tap, H. X. Vinh, H. T. Nguyen-Truong, J. B. Qiu, D. C. Zhou, N. M. Ty, *Opt. Mater.* **2019**, *95*, 109229.
- [92] P. K. Shahi, P. Singh, S. B. Rai, A. Bahadur, *Inorg. Chem.* **2016**, *55*, 1535.
- [93] D. Ghosh, S. Balaji, K. Biswas, K. Annapurna, *J. Appl. Phys.* **2016**, *120*, 233104.
- [94] L. J. Borrero-González, L. A. O. Nunes, G. S. Bianchi, F. B. G. Astrath, M. L. Baesso, *J. Appl. Phys.* **2013**, *114*, 013103.
- [95] Y. P. Tai, G. J. Zheng, H. Wang, J. T. Bai, *J. Photochem. Photobiol. A* **2015**, *303*, 80.
- [96] J. Zhao, X. Wang, Q. Pang, A. P. Zhang, *ECS J. Solid State Sci. Technol.* **2021**, *10*, 016004.
- [97] O. AitMellal, L. Oufni, M. Y. Messous, M. Tahri, S. Neatu, M. Florea, F. Neatu, M. Secu, *J. Mater. Sci.* **2022**, *33*, 4197.
- [98] R. A. Talewar, S. Mahamuda, A. S. Rao, V. M. Gaikwad, P. D. Belsare, S. V. Moharil, *J. Lumin.* **2020**, *222*, 117118.
- [99] Y. Tai, B. Pan, X. Li, Z. Nie, X. Du, G. Yuan, *RSC Adv.* **2018**, *8*, 37396.
- [100] P. Tumram, P. D. Sahare, S. V. Moharil, *J. Lumin.* **2018**, *199*, 78.
- [101] P. K. Tawalare, V. B. Bhatkar, S. K. Omanwar, S. V. Moharil, *Luminescence* **2018**, *33*, 1288.
- [102] A. Vyas, C. P. Joshi, P. D. Sahare, S. V. Moharil, *J. Alloy Compd.* **2018**, *743*, 789.
- [103] Z. J. Liu, J. Y. Li, L. Y. Yang, Q. Q. Chen, Y. B. Chu, N. L. Dai, *Sol. Energy Mater. Sol. C* **2014**, *122*, 46.
- [104] J. D. Chen, H. Guo, Z. Q. Li, H. Zhang, Y. X. Zhuang, *Opt. Mater.* **2010**, *32*, 998.
- [105] P. K. Tawalare, P. D. Belsare, S. V. Moharil, *Phys. Solid State* **2021**, *63*, 758.



Guoxiang Song received his B.S. degree from Henan Normal University and M.S. degree from Henan University. He is currently pursuing his Ph.D. at the School of Electronic Science and Engineering, Southeast University (China). His research focuses on spectral conversion materials and novel solar cells.



Chaogang Lou is a professor at Southeast University, China. He received his B.S. degree from Southeast University and Ph.D. degree from Aberdeen University in Electronic Engineering. Then, he worked as a postdoctoral fellow at Heriot-Watt University. His current research focuses on improving solar cells by spectral conversion and low-temperature thermophotovoltaic cells.



Han Diao received her B.S. degree from Nanjing University of Science and Technology (Nanjing, China) in 2016. She is currently pursuing her Ph.D. degree at the School of Electronic Science and Engineering, Southeast University (China). Her current research focuses on novel photovoltaic devices and luminescent materials.



Ruiqi Zhu is a master's student at Southeast University (China). She graduated from Nanjing Normal University with a B.S. degree in photoelectric information science and engineering in 2020. Her current research interests focus on photovoltaic materials for energy conversion and novel thermal photovoltaic cells.